AN EFFICIENT HAPTIC INTERFACE FOR A VARIABLE DISPLACEMENT PUMP CONTROLLED EXCAVATOR

A Thesis
Presented to
The Academic Faculty

by

Mark David Elton

In Partial Fulfillment
of the Requirements for the Degree
Master of Science in the
G. W. Woodruff School of Mechanical Engineering

Georgia Institute of Technology
May 2009

AN EFFICIENT HAPTIC INTERFACE FOR A VARIABLE DISPLACEMENT PUMP CONTROLLED EXCAVATOR

Approved by:

Dr. Wayne Book, Advisor
G.W. Woodruff School of Mechanical Engineering
Georgia Institute of Technology

Dr. Harvey Lipkin
G.W. Woodruff School of Mechanical Engineering
Georgia Institute of Technology

Dr. Chris Paredis
G.W. Woodruff School of Mechanical Engineering
Georgia Institute of Technology

Date Approved: March 25, 2009

To all those who have helped me see this through

ACKNOWLEDGEMENTS

I must first acknowledge Dr. Wayne Book, my advisor, for his guidance in my academic career and for his direction and support on this project. I have truly been privileged to work with him. I would also like to thank Dr. Chris Paredis and Dr. Harvey Lipkin for agreeing to serve on my committee and for their assistance in polishing my thesis. Also, I must thank J.D. Huggins for his assistance and advice, especially in the development of the test stand, and Dr. Matthew Kontz for the effort he took to make sure that I understood the technical details of his simulation and for the advice he gave, most of which I did not know I needed until much later.

A thanks is due to the Center for Compact and Efficient Fluid Power, the main sponsor of this project. Being part of the Center has introduced me to others working on related fluid power projects, including Chris Williamson and Josh Zimmerman who supplied me with data from their experiments. I have also received assistance from all of my lab mates at Georgia Tech, and want to thank them for their suggestions and insights, especially Aaron Enes and Longke Wang. I must also mention that generous in kind donations were made on behalf of the Bobcat Company by Scott Schuh and Jim Bruer.

I would like to thank my parents for the time, love, and sacrifices they made to raise me in a manner that has made my graduate education possible. Lastly, I would like to thank my wife, Hillary, for her patience, support, and love.

TABLE OF CONTENTS

LIST OF FIGURES

SUMMARY

Human-machine interfaces (HMIs) influence operator effectiveness and machine efficiency. Further immersion of the operator into the machine's working environment gives the operator a better feel for the status of the machine and its working conditions. With this knowledge, operators can more efficiently control machines. The use of multi-modal HMIs involving haptics, sound, and visual feedback can immerse the operator into the machine's environment and provide assistive clues about the state of the machine.

To test new HMIs, the standard and new interfaces must be tested against one another on machines doing the same task in the same environment. Changing the controls on a machine is time consuming and can be expensive. In order to bypass these difficulties, simulators are constructed so that different HMIs can easily be switched in and out for testing purposes and so that the environment is standardized for all tests.

This thesis develops a realistic excavator model that mimics a mini-excavator's dynamics and soil interaction during digging tasks. A realistic graphical interface is written that exceeds the quality of current academic simulators, such as [24] [28].The graphical interface and new HMI are placed together with a model of the excavator's mechanical and hydraulic dynamics into an operator workstation. The operator workstation is built as a tool for future tests and configured to allow new interfaces to be easily implemented and tested. Two coordinated control schemes are developed for a mini-excavator and preliminary tests are run to measure increases in operator effectiveness and machine efficiency. Force feedback is applied to both of the coordinated control schemes and the effectiveness and efficiency increases are measured again, to show that the operator workstation can be used to test new HMIs.

CHAPTER 1

INTRODUCTION

This thesis covers the development of an excavator simulator constructed for the measurement of the relative effectiveness of different human-machine interfaces (HMIs) and discusses the results from preliminary tests comparing four different HMIs.

Before the 1950's, HMIs were mainly ways to make it possible for a human to control a machine using only human-scale forces. With the invention of the first teleoperators, HMIs were no longer dependent on physical linkages from the controls to the machine hardware. This gave designers more freedom to create different controls to better match human capabilities to tasks. However, it was quickly discovered that operators depended on tactile feedback from the mechanical linkages to understand the state of the machine. For example, when the first aircraft controls were mechanically decoupled from ailerons and rudder by means of electrical motors (the origin of the phrase "fly-by-wire"), pilots no longer had a 'feel' for the control effort of the plane [1]. In this case and others, artificial means of feedback were created in order to give operators a 'feel' of what the machine was doing.

The field of haptics, which means "relating to or based on the sense of touch" focuses on giving touch-based or force feedback to a human operator in order to provide more information about the state of the machine being operated [2]. Haptics range from small devices, the most common current example is probably the vibrate function of a cell phone, to the very large, like the aircraft example discussed above. In this example, giving scaled force feedback to the pilot allows him to better control the plane. Better

control of an excavator can be measured in various ways. The metric for “better” control in this thesis is increased operator effectiveness and machine energy efficiency.

HMIs can improve efficiency and effectiveness by better matching human abilities to task’ demands. Excavators and other multi-degree of freedom devices have non-intuitive kinematics that require extensive operator training and experience to perfect. Coordinated control schemes create more intuitive interfaces that reduce training time and allow for better end-effector control.

More intuitive HMIs decrease the operator’s cognitive load, especially as the time spent completing the task increases [3]. Reducing the cognitive load reduces the number of errors and allows the same task to be completed in less time [3]. If the task is completed more quickly, time and money will be saved. Less time per task converts to less operator time to pay for, less machine wear and tear per task, less machine rental time, and shorter hold-ups for tasks waiting on the current task’s completion. HMIs also can increase machine efficiency by helping operators to move along more energy efficient trajectories. Less errors being commanded causes less fuel to be consumed and lower machine loads, which correspond to savings in fuel cost, lower emissions, and less wear and tear on the machine. All of these savings offset the costs of increased system complexity expenses, such as force feedback joysticks and increased computing power onboard.

This thesis focuses on the construction of an excavator simulator with a more realistic model then the current academic standard. Dynamic models of the excavator’s hydraulic and mechanical systems are developed from manufacturer data. A graphical interface is written in C++ using the OpenGL library and includes such features as trees,

shadows, and actual CAD models to elevate the degree of realism. A new soil model is created on a base of previous work but with additions to expand the soil model's capabilities so that it can calculate the bucket-soil interaction force for any trajectory.

A novel human-machine interface with a force feedback joystick to give the operator of a mini-excavator a sense of the digging forces, or to be more specific, the force being applied to the bucket by the environment, is construction using an off-the-shelf haptic joystick and writing an interface using C++. Improvements from haptic feedback in operator and machine efficiency are assessed to demonstrate the simulator's ability to be a test stand to test new HMIs, although the tests themselves are not statistically significant.

The thesis is arranges as follows: Chapter 2 gives a background and overview of previous work done on HMIs for hydraulically actuated multi-DOF machines. Chapter 3 discusses the excavator model and includes derivations of the mechanical linkage's kinematics and dynamics. The excavator's hydraulic system model and dynamics are discussed in detail as well. The final section of Chapter 3 covers the novel soil model that was developed for the simulation. Chapter 4 explains the HMIs and control schemes developed. Chapter 5 discusses the preliminary tests, both how the tests were performed and the test results. Chapter 6 offers a brief conclusion including the contributions of this project and possibilities for future work.

CHAPTER 2

BACKGROUND

Mobile hydraulic machinery, such as off-road construction, farming, and mining equipment, has had the same basic human-machine interface since its inception. For excavators, the four main functions are controlled by two two-DOF joysticks. Each degree of freedom controls the flow into the actuator (a hydraulic cylinder or motor) controlling the joint angle of a single link. The position of the joystick is roughly proportional to the resulting velocity of the actuator. The velocity of the actuators is kinematically related to the bucket tip velocity.

Since excavator kinematics are not intuitive, coordinated controllers were implemented both on excavators and other similar robotic arms [4-8]. Coordinated controllers mechanically decoupled the controls from the device and allowed the operator to either command a Cartesian position or velocity. Operator efficiency improved, especially among novices. Velocity control was found to be more effective for large scale motions, and position control was preferred for finer motions. Several switching or hybrid controllers have been suggested that switch between position and velocity control [9].

Haptics have been added to many different types of machines, but mainly to electrically actuated systems such as in [10]. [11] investigated using a haptic controller to aid operators of a log loader (an excavator with an attachment) to apply a commanded force. Their one-dimensional experiments showed that operators could more closely reproduce a commanded force using a ‘stiffness’ controller. [4] investigated using force

feedback to reduced log damage using a feller-buncher. Without haptic feedback, their results show that the operator has almost no control of the force applied at the end effector. With haptic feedback, operators reasonably tracked the commanded force. [12] used an impedance shaping haptic controller and showed that with its assistance backhoe operators could better detect stiff buried objects.

This thesis focuses on improvements in operator and machine efficiency caused by using a Phantom force feedback joystick to display the soil-bucket interaction forces during excavation with a simulated mini-excavator. Two different controller schemes, a position controller and a mixed position-velocity controller, are also tested with and without haptic feedback.

CHAPTER 3

SYSTEM MODELING

New human-machine interfaces must be mounted on the actual machine being controlled in order to test their true effectiveness. Changing the controls of a machine is time consuming and can be expensive. In order to be able to quickly interchange and test new HMIs, an excavator simulator is constructed that simulates the dynamics of the actual machine and its environment. The simulator can then be used to ascertain the effectiveness and efficiency improvements of the new HMI without the difficulties associated with implementing the new HMI on the actual machine.

The system modeled for the excavator simulator is a Bobcat 435 mini-excavator. Excavators have been previously modeled, so the excavator kinematics and dynamics discussed in this chapter are based on previous work. The literature does not have an accurate model of the 435 excavator, so with the assistance of the manufacturer and researchers at Purdue University, the necessary parameters for this simulation were measured so that the model would reflect the motion of the actual machine.

The model was broken into segments, pictured in Fig. 1, each of which is discussed in a later section. The input and output variables of each block and the blocks' interconnections are shown in Fig. 1.

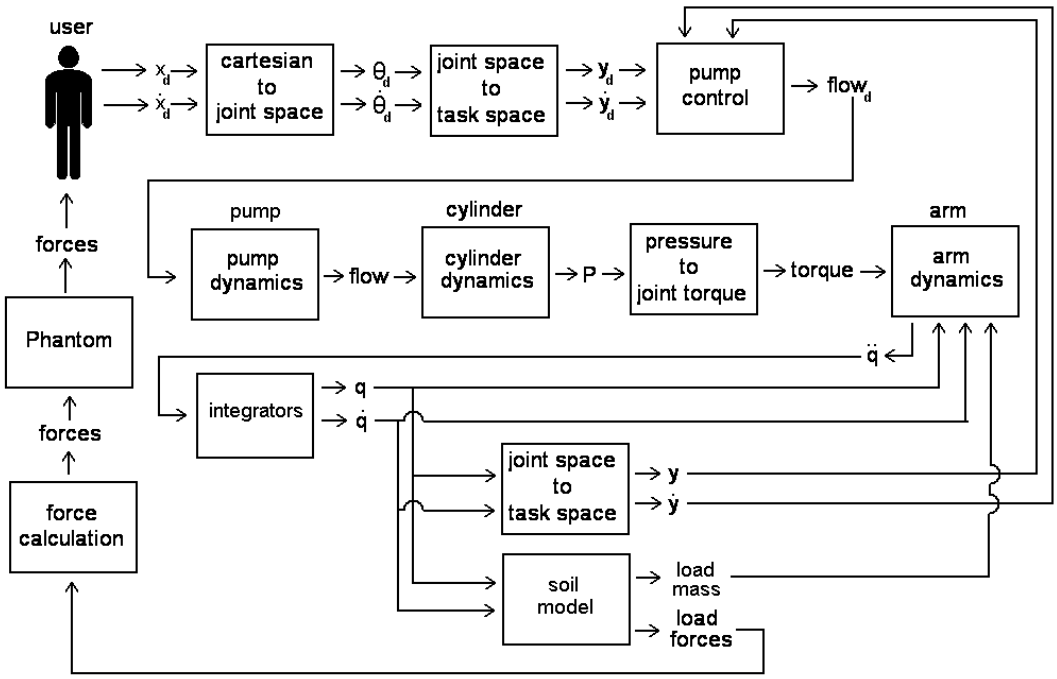

Fig. 1 System Diagram.

About the Bobcat 435 Excavator

The Bobcat 435 excavator is a five-ton machine powered by a 48.8 hp diesel engine (Fig. 2) [13]. It has five joints: the cab (or swing), an offset joint that adjust the angle of the arm relative to the cab, and the three joints of the arm itself: the boom, stick (also called the arm, but it is referred to as the stick in this work to differentiate it from all three links together being called the arm), and bucket (Fig. 3).

Fig. 2 Bobcat 435 Mini-Excavator in a Normal Dig Cycle.

It also is equipped with two tracks that can be operated independently to position the excavator and a blade that can be raised or lowered to increase machine stability or backfill trenches.

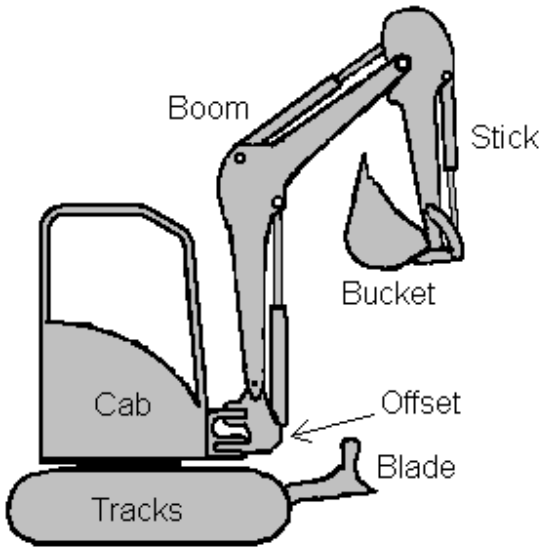

Fig. 3 Links of the Bobcat Mini-Excavator.

During a standard dig cycle, only four of the joints are used: the swing, boom, stick, and bucket. The offset joint is generally adjusted prior to excavation and, except in tight spaces, is set so that the arm faces directly ahead from the point of view of the operator. The tracks and swing are driven by hydraulic motors and all other links are actuated by hydraulic cylinders.

The Center for Compact and Efficient Fluid Power (CCEFP) sponsored a related project at Purdue University to study the efficiency difference between pump controlled and valve controlled machines. A standard valve controlled 435 machine was tested for efficiency and then the valves and fixed displacement pump were replaced by four variable displacement pumps. Each pump controlled one of the four main functions (swing, boom, stick, and bucket) and also drove one of the four lesser used functions (offset, blade, and left and right tracks) [14]. The variable displacement pump controlled excavator is modeled in this work, not the standard valve controlled excavator. The four minor functions are assumed not to be in use in the model, which is reasonable for normal dig cycles.

Kinematics

Definitions

Task Space – the states of the excavator are defined with relation to the Cartesian world frame with the origin fixed at O_0 (see Fig. 4). Using this space gives a Cartesian position and velocity for each point on the excavator. Task space contains the variables:

x, y, z – position

v_x, v_y, v_z – velocity

ω_x, ω_y, ω_z – angular velocity

Joint Space – the excavator states are defined in terms of joint positions, velocities, and accelerations. Joint space contains the variables

θ_i - angular position of joint i

$\dot{\theta}_i$ - angular velocity of joint i

$\ddot{\theta}_i$ - angular acceleration of joint i

Cylinder Space – the excavator states are defined in terms of the position and motion of the hydraulic actuators. This space's states are the actuators' positions and velocities.

y_k – the position of actuator k. For y_1 this is the same as θ_1

v_k – the velocity of actuator k. For y_1 this is the same as $\dot{\theta}_1$.

p_{ab} – the Cartesian vector between origins O_a and O_b.

r_{AB} – the Cartesian distance between points A and B. If A or B is a number then the point referred to is O_A or O_B. This is an absolute distance so $r_{AB} = r_{BA}$.

a_k – the length of link k, consistent with Denavit-Hartenberg notation (see Fig. 4).

a_1 = length of the cab

a_2 = length of the offset link

a_3 = length of the boom

a_4 = length of the stick

a_5 = length of the bucket

θ_k – the rotated angle of joint k, consistent with Denavit-Hartenberg notation (see Fig. 5)

θ_1 = rotation of the cab

θ_2 = rotation of the offset link

θ_3 = rotation of the boom

θ_4 = rotation of the stick

θ_5 = rotation of the bucket

θ_{ijk} – the positive angle less than 180^o formed by the line segments connecting points i and j and points j and k. If i, j, or k is a number, then the point being referred to is respectively origin O_i, O_j, or O_k.

The following refer only to joint angles of the machine, and not angles referred to as θ_{ijk}

c_i – $\cos(\theta_i)$

c_{ij} – $\cos(\theta_i + \theta_j)$

c_{ijk} – $\cos(\theta_i + \theta_j + \theta_k)$

s_i – $\sin(\theta_i)$

s_{ij} – $\sin(\theta_i + \theta_j)$

s_{ijk} – $\sin(\theta_i + \theta_j + \theta_k)$

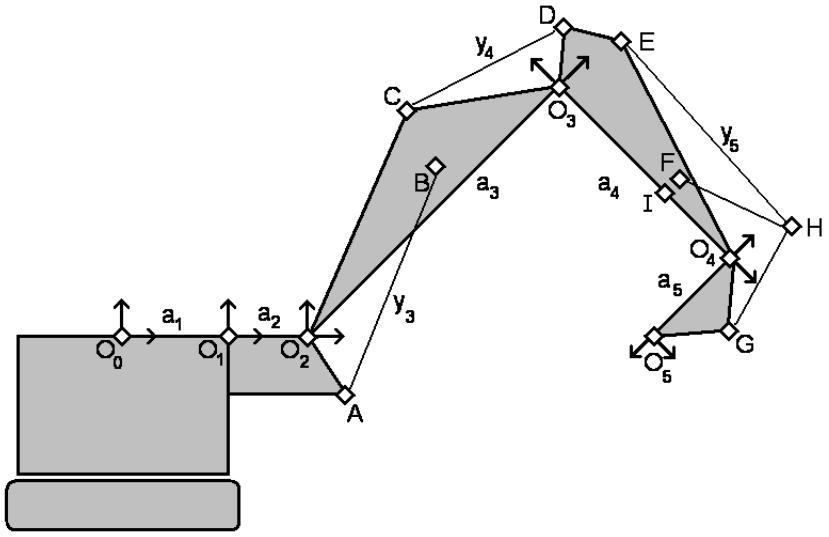

Fig. 4 Kinematic Points of Interest and Cylinder Link Lengths. O_i is the origin of frame i. a_i is the distance between O_{i-1} to O_i. The boom cylinder attaches at points A and B and is of length y_3. The stick cylinder extends between points C and D and is of length y_4. The bucket cylinder attaches to pins at point E and H and has length y_5. The four-bar mechanism attached to the bucket includes two links, on attaching point F and point H and another attaching point H and point G.

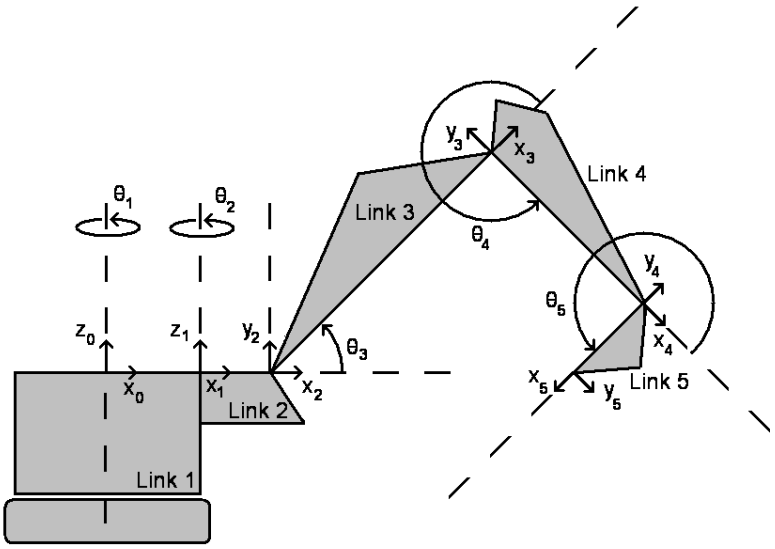

Fig. 5 Kinematic Origins and Joint Angles. Note that point I is the nearest point on $\overline{O_3O_4}$, or r_{34}, to point F, therefore $r_{IF} \perp r_{34}$. The variable y_i is used to designate the length of cylinder i, and should not be confused with the y-axis of each of frame. To avoid confusion, the cylinder lengths appear as a scalar, y_i, and the axes appear as a vector, $\vec{y}_i$. $[\vec{x}_i, \vec{y}_i, \vec{z}_i]$ is the coordinate frame associated with link i. θ_i is the rotation of link i about $\vec{z}_{i-1}$.

Joint Space to Task Space

The excavator kinematics are found using the excavator's Denavit-Hartenberg parameters to find the standard robotics Jacobian. The Jacobian allows for easy transformations between task space and joint space and vice versa. Although the joint space to task space transformation is not used in the excavator dynamics, it is included in the soil model and the force calculation block (see Fig. 1).

To go from a position in joint space to a position in task space is a brief exercise in geometry.

$$p_{00} = \begin{bmatrix} 0 \\ 0 \\ 0 \end{bmatrix} \tag{1}$$

$$p_{01} = \begin{bmatrix} a_1 c_1 \\ a_1 s_1 \\ 0 \end{bmatrix} \tag{2}$$

$$p_{02} = p_{01} + \begin{bmatrix} a_2 c_{12} \\ a_2 s_{12} \\ 0 \end{bmatrix} = \begin{bmatrix} a_1 c_1 + a_2 c_{12} \\ a_1 s_1 + a_2 s_{12} \\ 0 \end{bmatrix} \tag{3}$$

$$p_{03} = p_{02} + \begin{bmatrix} a_3 c_3 c_{12} \\ a_3 c_3 s_{12} \\ a_3 s_3 \end{bmatrix} = \begin{bmatrix} a_1 c_1 + a_2 c_{12} + a_3 c_3 c_{12} \\ a_1 s_1 + a_2 s_{12} + a_3 c_3 s_{12} \\ a_3 s_3 \end{bmatrix} \tag{4}$$

$$p_{04} = p_{03} + \begin{bmatrix} a_4 c_{34} c_{12} \\ a_4 c_{34} s_{12} \\ a_4 s_{34} \end{bmatrix} = \begin{bmatrix} a_1 c_1 + a_2 c_{12} + a_3 c_3 c_{12} + a_4 c_{34} c_{12} \\ a_1 s_1 + a_2 s_{12} + a_3 c_3 s_{12} + a_4 c_{34} s_{12} \\ a_3 s_3 + a_4 s_{34} \end{bmatrix} \tag{5}$$

$$p_{05} = p_{04} + \begin{bmatrix} a_5 c_{345} c_{12} \\ a_5 c_{345} s_{12} \\ a_5 s_{345} \end{bmatrix} = \begin{bmatrix} a_1 c_1 + a_2 c_{12} + a_3 c_3 c_{12} + a_4 c_{34} c_{12} + a_5 c_{345} c_{12} \\ a_1 s_1 + a_2 s_{12} + a_3 c_3 s_{12} + a_4 c_{34} s_{12} + a_5 c_{345} s_{12} \\ a_3 s_3 + a_4 s_{34} + a_5 s_{345} \end{bmatrix} \tag{6}$$

The standard Jacobian for a 5-link revolute joint robot is found by

$$J = \begin{bmatrix} z_0 \times (p_{05} - p_{00}) & z_1 \times (p_{05} - p_{01}) & z_2 \times (p_{05} - p_{02}) & z_3 \times (p_{05} - p_{03}) & z_4 \times (p_{05} - p_{04}) \\ z_0 & z_1 & z_2 & z_3 & z_4 \end{bmatrix}$$

For the 435 excavator

$$z_0 = z_1 = \begin{bmatrix} 0 \\ 0 \\ 1 \end{bmatrix} \qquad \text{and} \qquad z_2 = z_3 = z_4 = \begin{bmatrix} s_{12} \\ -c_{12} \\ 0 \end{bmatrix}$$

However, for ease of use, the operator commands the bucket angle and velocity, θ_5 and $\dot{\theta}_5$, independently of the position and velocity of the rest of the excavator. So the command consists of a Cartesian position and velocity for the wrist, O_4, and an angle and rotational velocity for the bucket. This decouples the excavator into two parts – one that

controls the wrist position and velocity and one that controls the bucket angle and velocity. So we need only find the Jacobian for the first four links of the excavator

$$J = \begin{bmatrix} z_0 \times (p_{04} - p_{00}) & z_1 \times (p_{04} - p_{01}) & z_2 \times (p_{04} - p_{02}) & z_3 \times (p_{04} - p_{03}) \\ z_0 & z_1 & z_2 & z_3 \end{bmatrix} \quad (7)$$

The Cartesian velocities can then be found from

$$v = J \cdot \dot{\theta} = J \cdot \begin{bmatrix} \dot{\theta}_1 \\ \dot{\theta}_2 \\ \dot{\theta}_3 \\ \dot{\theta}_4 \end{bmatrix} \quad (8)$$

where $v = \begin{bmatrix} v_x \\ v_y \\ v_z \\ \omega_x \\ \omega_y \\ \omega_z \end{bmatrix}$.

Task Space to Joint Space

Going from Cartesian space to joint space is slightly more difficult. The bucket is again ignored, so only the first four links of the excavator are examined (swing, offset, boom, and stick). The offset typically does not move during a dig cycle, and is generally set so that the arm of the excavator extends parallel to the operator's line of sight when facing forward (see Fig. 6)

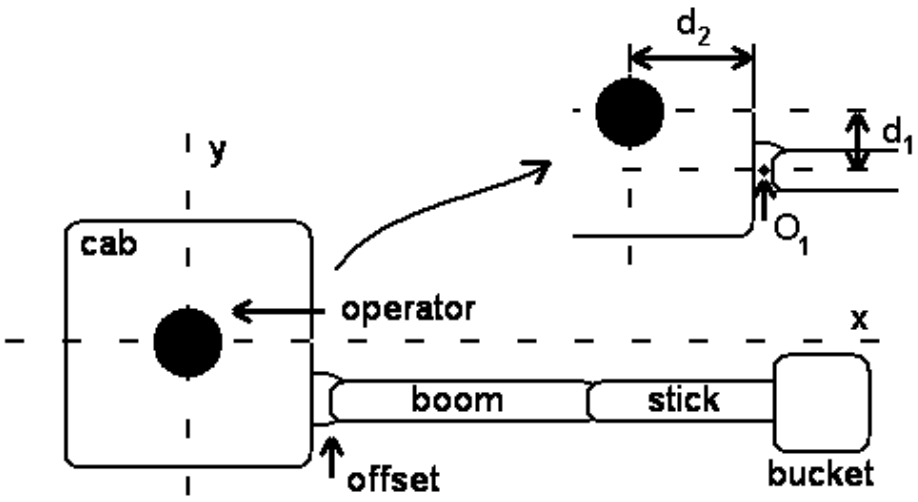

Fig. 6 Joint Space to Task Space Coordinate Frame.

The swing angle, θ_1, is found by positioning the cab so that the plane of the arm includes the desired point. If the desired point is $[x_d, y_d, z_d]$, then by defining two angles, γ and φ as

$$\varphi = \arctan\left(\frac{y_d}{x_d}\right)$$

$$\gamma = \arccos(d_1 / \sqrt{x_d^{\,2} + y_d^{\,2}})$$

then θ_1 is defined as being the angle that the cab rotates from the point where the operator is facing down the x-axis (in Fig. 6 $\theta_1 = 0^o$). Therefore

$$\theta_1 = -\frac{\pi}{2} + \gamma + \varphi \tag{9}$$

θ_2 is fixed and keeps the arm parallel to the x_1 axis, which means that θ_2 is constant. To find the other two joint angles, θ_3 and θ_4, we first must find p_{02} (see equation 3), and find the distance between it and the desired point.

$$\begin{bmatrix} x_r \\ y_r \\ z_r \end{bmatrix} = \begin{bmatrix} x_d \\ y_d \\ z_d \end{bmatrix} - p_{02} \tag{10}$$

Now the problem is reduced to a simple two-link revolute manipulator moving in the plane. To further simplify formulas, the following are defined:

$$d_r = \sqrt{x_r^2 + y_r^2 + z_r^2} \tag{11}$$

The angle that the arm must come up from the horizontal plane is

$$\phi = \arctan\left(\frac{z_r}{\sqrt{x_r^2 + y_r^2}} \right) \tag{12}$$

Solving the inverse kinematics equations gives

$$\theta_{423} = \frac{\arccos(a_3^2 + d_r^2 - a_4^2)}{2a_3 d_r}$$

$$\theta_{234} = \frac{\arccos(a_3^2 + a_4^2 - d_r^2)}{2a_3 a_4}$$

$$\theta_3 = \theta_{423} + \phi$$

$$\theta_4 = \theta_{234} - \pi$$

To convert from task space velocities to joint space velocities, we use

$$\dot{\theta} = J^{-1} \cdot v \tag{13}$$

This requires the inverse of J, and, since J is not square, it is not invertible. As mentioned previously, during normal operation the offset link does not move ($\dot{\theta}_2 = 0$). This allows the elimination of the second column of the Jacobian (see equation 7) since all of its values are multiplied by zero. The resulting 6x3 Jacobian can have no more than three independent rows. Since the Cartesian velocity is being controlled and not angular velocity, the top three rows are used to form a 3x3 Jacobian for the excavator swing, boom, and stick. This new 3x3 Jacobian has rank 3 and can be found by

$$J = \begin{bmatrix} z_0 \times (p_{04} - p_{00}) & z_2 \times (p_{04} - p_{02}) & z_3 \times (p_{04} - p_{03}) \end{bmatrix}$$

The Cartesian velocities can then be found from equation 8

where $v = \begin{bmatrix} v_x \\ v_y \\ v_z \end{bmatrix}$.

Joint Space to Cylinder Space

Cylinder space is the space containing the variables of the actuators. The swing motor position and velocity are linearly related to θ_1 and $\dot{\theta}_1$ by the gearing ratio, g_r. Instead of calculating the actual position and velocity of the motor, θ_1 and $\dot{\theta}_1$ are used as the task space variables as well as the joint space variables. The cylinder space variables for the swing motor are repetitive and somewhat meaningless since the swing motor is not a cylinder. For the other links actuated by cylinders, the cylinder positions and velocities are calculated in order to compute the hydraulic system dynamics.

Looking at Fig. 4, it is clear that

$$\theta_{A2B} = \theta_{B23} + \theta_3 + \pi - \theta_{A21} \tag{14}$$

Using the law of cosines to calculate the boom cylinder length gives

$$y_3 = \sqrt{r_{2A}^2 + r_{2B}^2 - 2r_{2A}r_{2B}\cos(\theta_{A2B})} \tag{15}$$

To find the cylinder velocity, the above equation is differentiated.

$$\dot{y}_3 = \frac{1}{2}\left(\sqrt{r_{2A}^2 + r_{2B}^2 - 2r_{2A}r_{2B}\cos(\theta_{A1B})}\right)^{-1} \cdot \left(2r_{2A}r_{2B}\sin(\theta_{A2B})\dot{\theta}_{A2B}\right) = \frac{r_{2A}r_{2B}\sin(\theta_{A2B})\dot{\theta}_{A2B}}{y_3}$$

By recognizing that $\dot{\theta}_{A2B} = \dot{\theta}_3$, the above equation is simplified to

$$\dot{y}_3 = \frac{r_{2A}r_{2B}\sin(\theta_{A2B})\dot{\theta}_3}{y_3} \tag{16}$$

For the stick cylinder, the equations are nearly identical except that the cylinder is now above the link rather than below it. By examining Fig. 4, we see

$$\theta_{C3D} = -\theta_{23C} - \theta_4 + \pi - \theta_{D34} \tag{17}$$

The law of cosines gives

$$y_4 = \sqrt{r_{3C}^2 + r_{3D}^2 - 2r_{3C}r_{3D}\cos(\theta_{C3D})} \tag{18}$$

Taking the time derivative and substituting $\dot{\theta}_{C3D} = \dot{\theta}_4$ gives the following

$$\dot{y}_4 = -\frac{r_{3C}r_{3DB}\sin(\theta_{C3D})\dot{\theta}_4}{y_4} \tag{19}$$

The bucket cylinder equations are more complex because of the linkage.

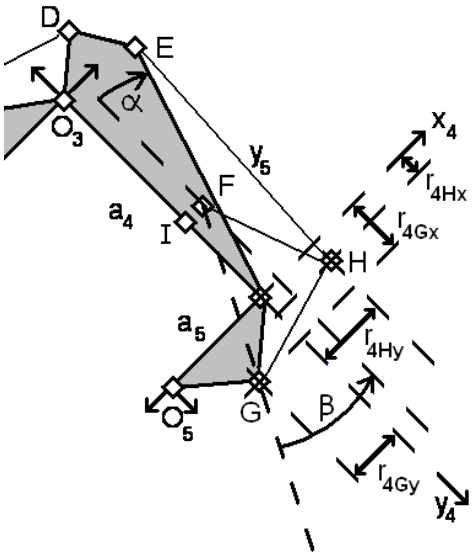

Fig. 7 Kinematic Variables of the Bucket Linkage. All dotted lines except $\overrightarrow{FG}$ are parallel to either $\overrightarrow{x_4}$ or $\overrightarrow{y_4}$.

Resolving r_{4G} into components along $\overrightarrow{x_4}$ and $\overrightarrow{y_4}$ (Fig. 7)

$$r_{4Gx} = r_{4G}\cos(\theta_5 + \theta_{G45}) \tag{20}$$

$$r_{4Gy} = r_{4G}\sin(\theta_5 + \theta_{G45}) \tag{21}$$

Therefore

$$r_{FG} = \sqrt{(r_{4I} + r_{4Gx})^2 + (r_{4Gy} - r_{FI})^2} \tag{22}$$

$$\beta = \arcsin\left(\frac{r_{4Gy} - r_{FI}}{r_{FG}}\right) \tag{23}$$

(see Fig. 7 for β definition)

Using the law of cosines

$$\cos(\theta_{GFH}) = \frac{r_{FH}^2 + r_{FG}^2 - r_{GH}^2}{2r_{FH}r_{FG}} \Rightarrow \theta_{GFH} = \arccos\left(\frac{r_{FH}^2 + r_{FG}^2 - r_{GH}^2}{2r_{FH}r_{RG}}\right) \tag{24}$$

This allows the calculation of θ_{EFH}

$$\theta_{EFH} = \pi - \alpha - \beta - \theta_{GFH} \tag{25}$$

And finally

$$y_5 = \sqrt{r_{EF}^2 + r_{FH}^2 - 2r_{EF}r_{FH}\cos(\theta_{EFH})} \tag{26}$$

To find the bucket cylinder velocity, the above equation is differentiated with respect to time. The only time varying variable in equation 26 is θ_{EFH}.

$$\dot{y}_5 = \frac{1}{2}\left(\sqrt{r_{EF}^2 + r_{FH}^2 - 2r_{EF}r_{FH}\cos(\theta_{EFH})}\right)^{-1}\left(2r_{EF}r_{FH}\sin(\theta_{EFH})\cdot\dot{\theta}_{EFH}\right)$$

θ_{EFH} is dependent on the time varying quantities θ_{GFH} and β. Their partial derivatives are:

$$\frac{\partial\theta_{GFH}}{\partial\theta_5} = \frac{(r_{FG} - r_{FH}\cos(\theta_{GFH}))(r_{FI}r_{4G}\cos(\theta_5 + \theta_{G45}) + r_{4I}r_{4G}\sin(\theta_5 + \theta_{G45}))}{r_{FH}r_{FG}^2\sin(\theta_{GFH})} = \frac{\dot{\theta}_{GFH}}{\dot{\theta}_5} \tag{27}$$

$$\frac{\partial \beta}{\partial \theta_5} = \frac{\left(r_{FG} + r_{FI}\sin(\beta)\right)\cdot r_{4G}\cos(\theta_5 + \theta_{G45}) + r_{4I}\sin(\beta)\cdot r_{4G}\sin(\theta_5 + \theta_{G45})}{r_{FG}^2\cos(\beta)} = \frac{\dot{\beta}}{\dot{\theta}_5} \tag{28}$$

$$\dot{\theta}_{EFH} = -\dot{\beta} - \dot{\theta}_{GFH} \tag{29}$$

Rearranging equation 28 and simplifying leads to

$$\frac{\dot{y}_5}{\dot{\theta}_{EFH}} = \frac{r_{EF}\, r_{FH}\sin(\theta_{EFH})}{y_5} = \frac{\partial y_5}{\partial \theta_{EFH}} \tag{30}$$

Then using the partials gives

$$\frac{\partial y_5}{\partial \theta_5} = \frac{\partial y_5}{\partial \theta_{EFH}}\left(\frac{\partial \theta_{EFH}}{\partial \theta_5}\right) = \frac{\partial y_5}{\partial \theta_{EFH}}\left(-\frac{\partial \beta}{\partial \theta_5} - \frac{\partial \theta_{GFH}}{\partial \theta_5}\right) = \frac{\dot{y}_5}{\dot{\theta}_5} \tag{31}$$

Substituting in the results from equations 27 and 28 gives the result

$$\dot{y}_5 = \frac{\partial \theta_5}{\partial y_5}\dot{\theta}_5 \tag{32}$$

Cylinder Space to Joint Space

As mentioned in the *Joint Space to Cylinder Space* section above, cylinder space only contains meaningful variables for those joints actuated by cylinders. The joint space coordinates are the same as the cylinder space coordinates for the swing motor.

For the cylinders, many of the same equations are used as transforming from joint space to cylinder space, they are simply used in a different order and rearranged to solve for a different variable.

For the boom cylinder, equation 15 is rearranged to read

$$\theta_{A2B} = \arccos\left(\frac{r_{2A}^2 + r_{2B}^2 - y_3^2}{2r_{2A}r_{2B}}\right) \tag{33}$$

Then by rearranging equation 14 to solve for θ_3 gives

$$\theta_3 = \theta_{A2B} - \theta_{B23} - \pi + \theta_{A21} \tag{34}$$

To find the joint velocity, the above equation could be differentiated, but this has already been done in equation 16. Solving for $\dot{\theta}_3$ in equation 16 renders

$$\dot{\theta}_3 = \frac{y_3 \dot{y}_3}{r_{2A} r_{2B} \sin(\theta_{A2B})} \tag{35}$$

The joint equations for the stick are similarly found by rearranging equations 17, 18, and 19

$$\theta_{C3D} = \arccos\left(\frac{r_{3C}^2 + r_{3D}^2 - y_4^2}{2 r_{3C} r_{3D}} \right) \tag{36}$$

$$\theta_4 = \pi - \theta_{C3D} - \theta_{C32} - \theta_{D34} \tag{37}$$

$$\dot{\theta}_4 = -\frac{y_4 \dot{y}_4}{r_{3C} r_{3D} \sin(\theta_{C3D})} \tag{38}$$

The four bar linkage that the bucket cylinder connects to makes the equations for θ_5 more complicated. Starting with the law of cosines

$$\theta_{EFH} = \arccos\left(\frac{r_{EF}^2 + r_{FH}^2 - y_5^2}{2 r_{EF} r_{FH}} \right) \tag{39}$$

The $\vec{x}_4$ and $\vec{y}_4$ components of r_{4H} and r_{FH} are designated with an additional subscript x or y. They are calculated by

$$r_{4Hx} = r_{4I} + r_{FH} \cos(\theta_{3FE} + \theta_{EFH}) \tag{40}$$

$$r_{4Hy} = r_{FI} + r_{FH} \sin(\theta_{3FE} + \theta_{EFH}) \tag{41}$$

$$r_{FHx} = r_{FH} \cos(\alpha + \theta_{EFH}) \tag{42}$$

$$r_{FHy} = r_{FH} \sin(\alpha + \theta_{EFH}) \tag{43}$$

By definition, this leads to

$$r_{4H} = \sqrt{r_{4Hx}^2 + r_{4Hy}^2} \tag{44}$$

$$\theta_{34H} = \arctan\left(\frac{r_{4Hy}}{r_{4Hx}}\right) \tag{45}$$

The law of cosines shows

$$\theta_{H4G} = \arccos\left(\frac{r_{4H}^2 + r_{4G}^2 - r_{GH}^2}{2r_{4H}r_{4G}}\right) \tag{46}$$

And finally,

$$\theta_5 = \pi - \theta_{34H} - \theta_{H4G} - \theta_{G45} \tag{47}$$

To find $\dot{\theta}_5$, start with equation 30

$$\frac{\dot{y}_5}{\dot{\theta}_{EFH}} = \frac{r_{EF}r_{FH}\sin(\theta_{EFH})}{y_5} = \frac{\partial y_5}{\partial \theta_{EFH}}$$

The derivative of equation 47 is

$$\dot{\theta}_5 = -\dot{\theta}_{34H} - \dot{\theta}_{H4G} \tag{48}$$

The partials of the two angles are

$$\frac{\partial \theta_{34H}}{\partial \theta_{EFH}} = \frac{r_{4I}r_{FHx} + r_{FI}r_{FHy} + r_{FH}^2}{r_{4H}^2} = \frac{\dot{\theta}_{34H}}{\dot{\theta}_{EFH}} \tag{49}$$

$$\frac{\partial \theta_{H4G}}{\partial \theta_{EFH}} = \frac{(r_{FI}r_{FHx} - r_{4I}r_{FHy})(r_{4G}\cos(\theta_{H4G}) - r_{4H})}{r_{4H}^2 r_{4G}\sin(\theta_{H4G})} = \frac{\dot{\theta}_{H4G}}{\dot{\theta}_{EFH}} \tag{50}$$

To find $\dot{\theta}_5$, the above equations are substituted into

$$\frac{\partial \theta_5}{\partial y_5} = \frac{\partial \theta_5}{\partial \theta_{EFH}}\left(\frac{\partial \theta_{EFH}}{\partial y_5}\right) = \frac{\partial \theta_{EFH}}{\partial y_5}\left(-\frac{\partial \theta_{34H}}{\partial \theta_{EFH}} - \frac{\partial \theta_{H4G}}{\partial \theta_{EFH}}\right) = \frac{\dot{\theta}_5}{\dot{y}_5} \tag{51}$$

The result is

$$\dot{\theta}_5 = \frac{\partial \theta_5}{\partial y_5} \dot{y}_5$$

Excavator Dynamics

The machine dynamics are calculated using the Newton-Euler formulation. They are not covered in detail here, but can be found in [15]. For ease of discussion, the equations will be written in the Lagrangian formulation.

$$[M(\theta)] \cdot [\ddot{\theta}] = [\mathrm{T}] - [C(\theta, \dot{\theta})] \tag{52}$$

[M] is the inertia matrix that includes gravitational terms. [$\ddot{\theta}$] is a vector of the joint accelerations. [T] is a vector of applied joint torques resulting from the actuator forces. [C] is a vector that includes Coriolis and friction terms and externally applied forces and moments from striking objects in the environment such as the ground. Since the offset joint is stationary, the applied torque about joint two negates any applied forces, moments and Coriolis terms. The second row and column are removed from [M] and the second term is removed from [T], [C], and [$\ddot{\theta}$]. Equation 52 is reduced to four simultaneous equations and is rewritten as

$$[\ddot{\theta}] = [M(\theta)]^{-1} ([\mathrm{T}] - [C(\theta, \dot{\theta})]) \tag{53}$$

The simulator solves for [$\ddot{\theta}$] in equation 53 and then integrates twice to find [$\dot{\theta}$] and [θ]. This is straightforward if the joint angles are within the limits of the machine. If a joint reaches its limit, the applied torque for that joint is no longer known since there is an unknown normal force being applied by the mechanical stop.

In this case, the integrators are set so that if the maximum joint angle is reached, the output value of the second integrator (integrating [$\dot{\theta}$] to get [θ]) is set to the

maximum joint angle, and the output of the first integrator (integrating [$\ddot{\theta}$] to get [$\dot{\theta}$]) is set to zero if $\dot{\theta}$ is positive. If $\dot{\theta}$ is negative, then no change is made. If the minimum joint angle is reached, the output value of the second integrator is set to the minimum joint angle, and the output of the first integrator (integrating [$\ddot{\theta}$] to get [$\dot{\theta}$]) is set to zero if $\dot{\theta}$ is negative. If it is positive, then no change is made.

In both cases, the joint accelerations are calculated as usual. If the joint angle is at its maximum and the calculated joint acceleration is positive, or if the joint angle is at its minimum and the calculated joint acceleration is negative, then the joint acceleration for that joint is set to zero and the corresponding row and column are removed from [M] and the corresponding term is removed from [T], [C], and [$\ddot{\theta}$]. Then the calculations are redone on the reduced equations. The result is again checked to see if any of the accelerations would cause the link to move beyond its limit, and if so, the equations are reduced in order again and the process is repeated.

In the case that two or more joint angles are at their limits and the joint accelerations cause the links to move past their limits, the terms corresponding to the farther out link are removed from the equation and the joint acceleration is set to zero for only that link. Then the reduced equation is solved and the process is repeated as necessary. Fig. 8 tabulates the logic for the joint states when joint i reaches its limit.

calculated θ_i	calculated $\dot{\theta}_i$	calculated $\ddot{\theta}_i$	limited θ_i	limited $\dot{\theta}_i$	limited $\ddot{\theta}_i$
$\theta_i \geq \theta_{max\,i}$	$\dot{\theta}_i \geq 0$	$\ddot{\theta}_i \geq 0$	$\theta_i = \theta_{max\,i}$	$\dot{\theta}_i = 0$	$\ddot{\theta}_i = 0$
		$\ddot{\theta}_i < 0$			
	$\dot{\theta}_i < 0$	$\ddot{\theta}_i \geq 0$		no change	
		$\ddot{\theta}_i < 0$			
$\theta_i \leq \theta_{min\,i}$	$\dot{\theta}_i > 0$	$\ddot{\theta}_i > 0$	$\theta_i = \theta_{min\,i}$	no change	
		$\ddot{\theta}_i \leq 0$			
	$\dot{\theta}_i \leq 0$	$\ddot{\theta}_i > 0$		$\dot{\theta}_i = 0$	
		$\ddot{\theta}_i \leq 0$			

Fig. 8 Joint State Limitations.

Hydraulic System Dynamics

The hydraulic system consists of four identical circuits shown in Fig. 9. Each circuit has its own pump and all four pumps are powered by the same diesel motor. The swing motor circuit has a hydraulic motor instead of a cylinder as pictured in Fig. 9.

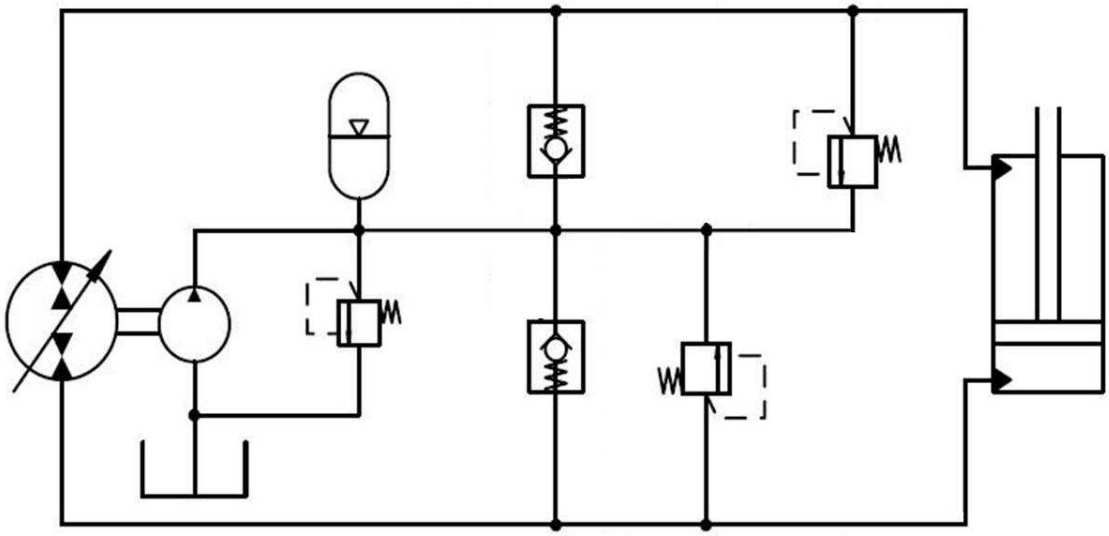

Fig. 9 Hydraulic Circuit for Each of the Four Variable Displacement Pumps.

Symbols

A_{hk} –Head-side area of piston k.

A_{rk} – Rod-side area of piston k.

P_{hk} – Pressure on the head side of actuator k. For the swing motor, the head side is defined as the side that must be pressurized to increase θ_1.

P_{rk} – Pressure on the rod side of actuator k. For the swing motor, the rod side is defined as the side that must be pressurized to decrease θ_1.

Q_{pk} – Flow from pump k that goes to actuator k. Note that k can only be 1, 3, 4, or 5 since joint 2 (offset) is not actuated during the dig cycle.

Q_{hk} - Flow into the head side of actuator k.

Q_{rk} - Flow into the rod side of actuator k.

Q_{Lk} – Internal leakage of actuator k. Postive Q_L means fluid flows across the piston from the head side to the rod side.

Q_{motor} – Flow through the swing motor.

L_k – Coefficient of internal leakage for actuator k.

g_r – Gear ratio of the swing motor gear to the cab ring gear.

v_{motor} – Velocity of the swing motor in rad/sec.

v_k – Velocity of cylinder k

V_{rev} – Swing motor displacement per revolution.

V_{hk} – Total volume of fluid between the pump and the piston on the head side of actuator k.

V_{rk} – Total volume of fluid between the pump and the piston on the rod side of actuator k.

V_{linehk} – Volume of the hose connecting the pump to the head side of actuator k.

V_{linerk} – Volume of the hose connecting the pump to the rod side of actuator k.

T_s – Sampling time period.

y_k – Overall length of cylinder k (from the connecting pin of the rod to the connecting pin of the cylinder)

y_{maxk} - Maximum y_k possible for cylinder k.

y_{mink} - Minimum y_k possible for cylinder k.

$stroke_k$ –Stroke length of cylinder k

pt_k – Piston thickness of cylinder k

β – Effective fluid bulk modulus.

τ_k – Torque about joint k. Positive torque is defined according to the right hand rule about $\vec{z}_k$

F_k – Force exerted by cylinder k

F_{ck} – Coulombic friction coefficient for actuator k

F_{vk} – Viscous friction coefficient for actuator k

C_k – Relationship between F_k and τ_k and between $\dot{y}_k$ and $\dot{\theta}_k$

Hydraulic Motor

The cab swing is actuated by a hydraulic motor which is driven by a variable displacement pump. The pump is a flow source that causes a pressure difference across the motor. The pressure differential causes the motor to rotate and fluid to flow from one side to the other. This flow, Q_1, is calculated first.

The flow due to internal leakage, Q_{L1}, is modeled as being linearly dependent on the pressure differential.

$$Q_{L1} = L_1(P_{h1} - P_{r1})$$

The flow through the motor is dependent on the motor velocity, gear ratio (g_r) and the displacement per revolution of the swing motor (V_{rev})

$$v_{motor} = \frac{\dot{\theta}_1}{2\pi} g_r$$

$$Q_{motor} = v_{motor} \cdot V_{rev}$$

Using the above, and knowing the pump flow, the head and rod side flows are calculated.

$$Q_{h1} = Q_{p1} - Q_{motor} - Q_{L1}$$

$$Q_{r1} = -Q_{p1} + Q_{motor} + Q_{L1}$$

Here $Q_{h1} = -Q_{r1}$ because the external leakage is assumed to be zero. This is not true. However, measurements at Purdue show that the external leakage of the swing motor is on the order of 10^{-13} m^3/s, and is therefore negligible compared to the pump flow [16].

The head side and rod side volumes of the swing motor vary with time and are difficult to measure. No attempt was made by researchers at Purdue to measure the volume of the motor, and it is assumed to be negligible when compared to the volume of the lines connecting the pump and motor. Therefore

$$V_{h1} = V_{lineh1} \qquad \text{and} \qquad V_{r1} = V_{liner1}$$

Using the effective fluid bulk modulus, β, near the median of several different measured values [17] gives

$$\dot{P}_{h1} = \frac{\beta}{V_{h1}} Q_{h1} \qquad \text{and} \qquad \dot{P}_{r1} = \frac{\beta}{V_{r1}} Q_{r1}$$

A simple rectangular integration technique allows for the discrete time calculation of the pressure.

$$P_{h1}(t+T_s) = P_{h1}(t) + \dot{P}_{h1}T_s \qquad \text{and} \qquad P_{r1}(t+T_s) = P_{r1}(t) + \dot{P}_{r1}T_s .$$

P(t) is the current pressure and P(t + T_s) is the pressure at the next time step.

Hydraulic Cylinder

Many of the dynamic equations of the hydraulic cylinders are similar to the hydraulic motor except that the flows and volumes are dependent on cylinder position and velocity rather than on motor velocity. Since cylinders actuate joints 3, 4, and 5, the subscript *k* in these equations must be either 3, 4, or 5. The leakage is calculated the same as for the hydraulic motor.

$$Q_{Lk} = L_k(P_{hk} - P_{rk}) \tag{54}$$

The external leakage measured at Purdue was found to be on the order of 10^{-13} m^3/s, and again is neglected [18]. The flows into the head and rod sides of the cylinders are

$$Q_{hk} = Q_{pk} - A_{hk}v_k - Q_{Lk} \qquad \text{and} \qquad Q_{rk} = -Q_{pk} + A_{rk}v_k + Q_{Lk} .$$

The volumes on the head and rod sides are

$$V_{hk} = A_{hk}(y_k + stroke_k + pt_k - y_{\max k}) + V_{linehk} \tag{55}$$

$$V_{rk} = A_{rk}(y_{\min k} + stroke_k - y_k) + V_{linerk} \tag{56}$$

Using the above equations

$$\dot{P}_{hk} = \frac{\beta}{V_{hk}}Q_{hk} \qquad \text{and} \qquad \dot{P}_{rk} = \frac{\beta}{V_{rk}}Q_{rk} .$$

A simple rectangular integration technique allows the calculation of the pressure. P(t) is the current pressure and P(t + T_s) is the pressure at the next time step.

$$P_{hk}(t+T_s) = P_{hk}(t) + \dot{P}_{hk}T_s \qquad \text{and} \qquad P_{rk}(t+T_s) = P_{rk}(t) + \dot{P}_{rk}T_s \,.$$

Pressure Relief and Check Valves

Each actuator is connected to a pressure relief valve on each side. Pressure relief valves connect the line to the tank and open if the line pressure exceeds a set point. The check valves are connected in the opposite direction and open if the line pressure drops below the charge pressure supplied by the charge pump (See Fig. 9).

The dynamics of these valves are complicated and not included in the model of the hydraulic system dynamics. They effectively act as limiters. If the pressure exceeds the set point of the pressure relief valve, then the valve is assumed to open instantaneously and pressure in the line assumed to be the set point of the valve. If the pressure drops below the charge pressure, then the check valve is assumed to open instantaneously and the pressure in the line is assumed to be the nominal charge pump pressure.

Pump Dynamics

The variable displacement pumps that replace the valves and fixed displacement pump are test pumps donated to Purdue by Parker. The maximum displacement is 18 cc/rev. Modeling a new pump is difficult and researchers at Purdue are not finished. In order to proceed, a first order lag is used as a model for the pump. The equation used is

$$Q(t+T_s) = Q(t) + \tau(Q_d(t) - Q(t))T_s \tag{57}$$

where Q(t) is the output flow of the pump at the current time, $Q(t+T_s)$ is the output flow of the pump during the next time step, $Q_d(t)$ is the desired, or commanded flow at the current time, T_s is the sampling time period, and τ is the time constant. Purdue reports that the pumps can go from zero flow to full flow in 80ms. τ is found from taking 63% of that value. The diesel engine is assumed to supply enough power to drive all pumps at full flow with maximum pressure differential at the workports of all the pumps. So far researchers have not found any exceptions to this assumption [16, 18].

Fluid Lines

The hoses and other fluid lines are also not modeled. The only effect taken into consideration from the lines is their contribution to the effective fluid bulk modulus and the fluid volume they hold, which is assumed to be constant. Any pressure drop over the length of the line is neglected, an assumption that still needs to be verified at Purdue,

Pressure to Torque Conversion

The output of the hydraulic actuator dynamics is the head and rod side pressures. To be useful in computing the excavator dynamics, the pressures must be converted into joint torques. Researchers at Purdue University measured the friction of each actuator as a function of actuator velocity and found it was best modeled as a combination of viscous and Coulombic friction.

For the swing motor

$$\tau_1 = \left(\frac{V_{rev}}{2\pi}\right)(P_{h1} - P_{r1}) - F_{v1}\dot{\theta}_1 - F_{c1}sign(\dot{\theta}_1) \tag{58}$$

The force exerted by cylinders 3, 4, and 5 is

$$F_k = P_{hk}A_{hk} - P_{rk}A_{rk} - \dot{y}_k F_{vk} - sign(\dot{y}_k)F_{ck} \tag{59}$$

Since the cylinder velocity vector and the cylinder force vector act along the same line causing a joint velocity and joint torque about the same point, the relationship between cylinder velocity and joint velocity is the same as between joint torque and cylinder force.

$$\frac{\dot{y}_k}{\dot{\theta}_k} = C_k = \frac{\tau_k}{F_k} \tag{60}$$

The C_k's are calculated, although not explicitly, in equations 16, 19, and 30

For the boom:

$$C_3 = \frac{r_{2A} r_{2B} \sin(\theta_{A2B})}{y_3} \tag{61}$$

For the stick:

$$C_4 = -\frac{r_{3C} r_{3DB} \sin(\theta_{C3D})}{y_4} \tag{62}$$

For the bucket:

$$C_5 = \frac{r_{EF} r_{FH} \sin(\theta_{EFH}) \cdot \dot{\theta}_{EFH}}{y_5} \tag{63}$$

Soil Model

Soil is difficult to model since its parameters vary greatly from type to type and within a single type from day to day (e.g. water content changes). In the simulator, the soil is modeled as a homogeneous substance with all necessary parameters known. The soil model is based upon previous work [19 - 22] and mainly on the work done by [23, 24]. These models all only examine trajectories where the bucket is coming towards the operator. No model for a bucket being pushed backwards, sideways, or any other direction than teeth-first though the soil exist in the literature. The model developed here

covers all of these possible scenarios. Also all previous soil simulations have only examined trajectories and soils where the soil can only exert a force on the bucket less than the force exerted on the soil by the bucket. The model developed here allows the force applied by the soil to exceed the applied bucket force, which is necessary to create a realistic simulation of digging. The new model also includes a section on wrist-soil interaction forces, an interaction not previously included in any model in the literature.

The soil is analyzed in cylindrical coordinates, but instead of using the standard radial and z directions, a new coordinate system is defined by the position of the teeth and flat of the bucket. One direction is tangential to the flat of the bucket, $\vec{t}$, and the other is normal to the flat of the bucket, $\vec{n}$. $\vec{\theta}$ is into the page in Fig. 10.

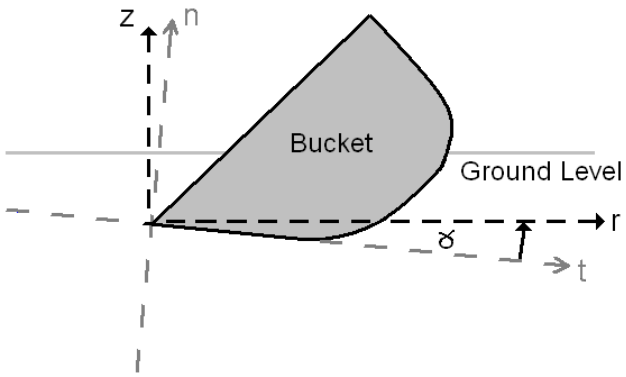

Fig. 10 Soil Coordinate System.

Previous work shows that the soil tends to shear along a plane dependent on the tool shape. [21, 23]. For this simulation, the soil was assumed to shear perpendicular to the flat of the bucket, along the *n*-axis. The soil shears when F_n exceeds F_{shear}.

$$F_{shear} = W \cdot d \cdot S \tag{64}$$

where W is the width of the bucket, d is the distance from the tip of the bucket to the point where the $\vec{n}$ axis breaks the surface of the soil, and S is the shear strength of the soil.

Bucket Moving Teeth First Through the Soil

The force exerted on the bucket while moving through the soil is modeled as a spring and damper. As the bucket moves through the soil, the stress in the soil increases prior to the soil shearing, which is modeled as the spring compressing. When it shears, the stress is relieved, and the soil exerts zero force on the bucket. The spring force resets to zero every time the soil shears. If [t_c, n_c, θ_c] is the most recent spot where the soil sheared, and [t, n, θ] is the current bucket tip position, the spring force exerted along $\vec{n}$ by the bucket is

$$F_{spring\_n} = k_n(n_c - n) \tag{65}$$

And similarly in the other two directions

$$F_{spring\_t} = k_t(t_c - t) \tag{66}$$

$$F_{spring\_\theta} = k_\theta(\theta_c - \theta) \tag{67}$$

k_n, k_t, and k_θ are the soil spring constants.

The damping forces of the soil on the bucket are similarly calculated. If S_p is the length of the flat of the bucket in the soil and the b's are the damping coefficients of the dirt with the subscript denoting the axis that the force acts along, the damping forces exerted by the soil on the bucket are

$$F_{soilt} = k_t(t_c - t) - S_p b_t v_{tipt} \tag{68}$$

$$F_{soil\,n} = k_n(n_c - n) - S_p b_n v_{tipn} \tag{69}$$

$$F_{soil\theta} = k_\theta(\theta_c - \theta) - S_p b_\theta v_{tip\theta} \tag{70}$$

The velocity of the bucket tip, v_{tip}, carries the 'tip' subscript to differentiate it from v, the velocity of the wrist used earlier. The spring constant along the θ-axis is much greater than the constant along the other axes since it is much more difficult to force the sidewall of the bucket through the soil. The moments exerted by the soil on the bucket in the $\vec{x}_0$ and $\vec{y}_0$ directions are respectively

$$M_{soilx} = S_p\left(k_{yx}(\gamma_c - \gamma)\sin(\theta_1) - b_{yx}\dot{\theta}_5\cos(\theta_1)\right) \tag{71}$$

$$M_{soily} = S_p\left(-k_{yy}(\gamma_c - \gamma)\cos(\theta_1) + b_{yy}\dot{\theta}_5\sin(\theta_1)\right) \tag{72}$$

The moment about $\vec{z}_0$ is not calculated since the bucket can not rotate independent of the excavator arm about the z_0-axis (any rotation about $\vec{z}_0$ is caused by changes in θ_1 and θ_2). γ_c is the angle of attack of the bucket at the last time the soil sheared (See γ in Fig. 10).

Small Bucket Retractions

In previous work, the spring constant has always been constant. In the model proposed here, the spring constant changes depending on the direction of the velocity of the bucket relative to the vector from last shearing point to the current bucket tip position. If the bucket continues on in the direction that it is headed then the stress continues to grow and the spring constant remains constant. If not, then the bucket is moving in a direction where the bucket teeth are not the first surface to contact the soil.

The damping from the soil is independent of the direction of travel since the drag force is caused by the soil sliding against the walls and bottom of the bucket. However, the spring force is mainly caused by the teeth pushing against the soil. Therefore, if the bucket reverses direction only a small amount (< ½ inch) in the n, t, or θ directions after

penetrating the soil, since the soil is deformable, the spring effect of the soil is greatly reduced in that direction. For this simulation, k_n, k_t, and k_θ are reduced by an order of magnitude. The reduction of the spring constants is necessary for stability when the bucket nears the equilibrium point in the soil (where the forces and moments applied at the bucket tip by the actuators equal the forces and moments applied by the soil). If the spring constants are truly constant, energy can be added to the system because the system is run in discrete time and the allowable sampling rate is limited by the available computing power. The discrete time system allows the bucket to penetrate farther into the soil beyond the equilibrium point then it could in a continuous time system. This compresses the spring farther than is actually possible for the excavator, adding energy to the system beyond what the actuators contribute. The extra energy causes unstable oscillations around the equilibrium point.

Bucket Moving Teeth Last Through the Soil

The previous section discussed small scale retractions of the bucket after it penetrated the soil. This section covers larger scale motions of the bucket where the bucket teeth are not the first bucket surface to contact the soil, for example, when the operator pushes the flat of the bucket down/backwards against the soil. These motions do not necessarily cause the teeth of the bucket to be the absolute last part of the bucket moving through the soil, but they will all be grouped together as “teeth last” motions of the bucket

Since the teeth are not preceding the flat of the bucket, the flat of the bucket is not necessarily clear of the soil. The soil that it comes in contact with exerts a force on the flat of the bucket. If $[t_{soil}, n_{soil}, \theta_c]$ is the first spot where the flat of the bucket contacted

the soil, and [t, n, θ] is the current position of the flat of the bucket, then the forces are found by

$$F_{spring\_n} = k_\theta (n_{soil} - n) \tag{73}$$

$$F_{spring\_t} = k_\theta (t_{soil} - t) \tag{74}$$

$$F_{damp\_n} = -A_b \sin(\varphi) b_\theta v_{tipn} \tag{75}$$

$$F_{damp\_t} = -A_b \cos(\varphi) b_\theta v_{tipt} \tag{76}$$

Note that the stiffer spring and damping constants, k_θ and b_θ are used since the back of the bucket moves through the soil in a manner more similar to side of the bucket than the teeth. A_b is the area of the bucket in contact with the soil, and is a function of S_p. φ is the same angle referred to in equation 9. For a full discussion of the soil model, see [25].

Wrist-Soil Forces

Another possible situation not dealt with in the literature, perhaps because it is uncommon, is when the wrist of the excavator strikes the ground first. This can happen if the bucket is retracted and the arm extended, such as in cases where the operator is trying to dig at the maximum arm length. When the wrist contacts the soil, the soil is modeled the same as above, but the interaction forces are calculated in [x,y,z] coordinates.

$$F_{spring\_x} = k_\theta (x_{soil} - x) \tag{77}$$

$$F_{spring\_y} = k_\theta (y_{soil} - y) \tag{78}$$

$$F_{spring\_z} = k_\theta (z_{soil} - z) \tag{79}$$

$$F_{damp\_x} = -A_{wx} b_\theta v_{wristx} \tag{80}$$

$$F_{damp\_y} = -A_{wy} b_\theta v_{wristy} \tag{81}$$

$$F_{damp\_z} = -A_{wz} b_\theta v_{wristz} \tag{82}$$

Notice the k_θ and b_θ are used since the wrist is a blunt object. $[x_{soil}, y_{soil}, z_{soil}]$ is the position where the wrist first comes into contact with the ground, whereas [x, y, z] is the current position of the wrist. A_{wx} is the area of the wrist in contact with the ground in the yz-plane, and similarly for A_{wy}, and A_{wz}. These forces are applied to the wrist in the Newton-Euler formulation of the machine dynamics in the excavator simulator.

Soil in the Bucket

The soil outside the trench area can be penetrated by the bucket; however it cannot be picked up by the bucket, so the soil level is always the same. In the trench, the soil level changes as the bucket teeth pass through it. The trench is made up of 256 discrete sections, each of which has a depth associated with it (see Fig. 25). The volume of the soil removed from each section of the trench is the product of the width of each section of the trench, Δs; the width of the trench, W_{trench}; and the difference between the previous and current depths, ΔD. For the volume of the entire load, all of these products are summed.

$$V_{load} = \sum_{k=1}^{256} \Delta D_k \cdot W_{trench} \cdot \Delta s \tag{83}$$

As the soil piles up in the bucket, the inertia of the bucket changes. The dirt is assumed to pile evenly across the bucket. If the inertia tensor, I_b, of the empty bucket is defined as

$$I_b = m_b J \tag{84}$$

where m_b is the mass of the bucket and J is a pseudo-inertia tensor [26]. The new tensor used in the excavator dynamics is calculated as

$$I_b = (m_b + m_s) \cdot J \tag{85}$$

with m_s being the mass of the soil in the bucket. Since m_s is of the same order or smaller as m_b, this estimation is allowable.

CHAPTER 4

CONTROL

The standard joysticks controlling the velocity of cylinders and swing motor are replaced with a Phantom 6-DOF joystick that the operator manipulates to give a position and velocity command to the simulation. A C++ interface program is written to facilitate communication between the Phantom and excavator simulator, but it is not covered here other than to say that it allowed the data transmission pictured in Fig. 26. This chapter discusses the force feedback schemes that were developed for use with the Phantom.

About the Phantom

Phantom devices are commercially available 3- to 6-DOF joysticks with three degrees of force feedback freedom manufactured by Sensable Technologies [27]. For this work, a Phantom Premium 1.0 is used (Fig. 11). The Phantom Premium 1.0 (or for simplicity in this work, Phantom) is constructed of three actuated links connected serially by revolute joints. A force of up to 8.5N is displayed at the end of the third link. For this project, four degrees of freedom are necessary, and so Sensable's encoder stylus gimbal is attached at the end of the third link, which becomes the wrist of 6-DOF joystick. The gimbal has three additional rotational degrees of freedom, but no additional force feedback mechanisms. Since the operator only controls four functions in the simulation, only one of the additional gimbal degrees of freedom is used. The other two degrees of freedom of the gimbal can be moved, but this information is discarded and not used. However, one of the additional degrees of freedom allows the Phantom handle to easily rotate between a left and right handed position. To switch from a right to left handed

orientation or vice versa, the position and velocity command from the gimbal needs simply to be negated. Two different coordinated control modes are implemented with the Phantom: position control mode and hybrid control mode.

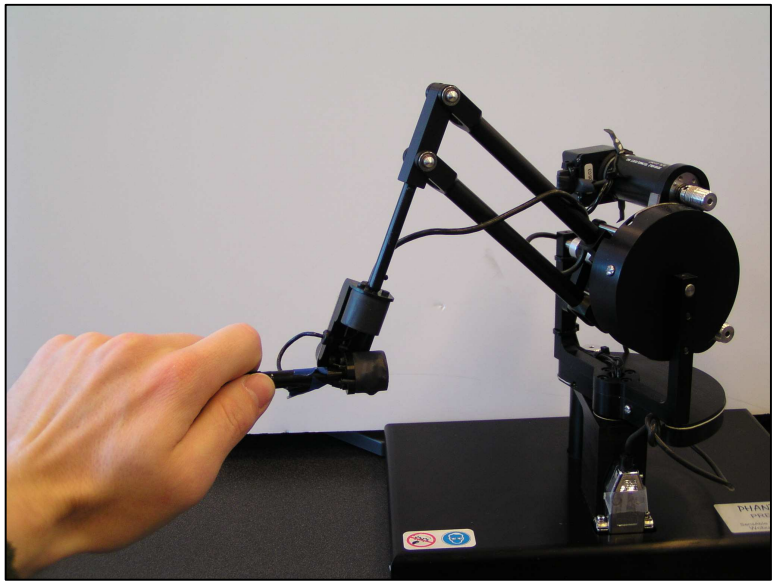

Fig. 11 Sensable PHANToM Premium 1.0 with the Gimbal Attachment.

Position Control Mode

For position control, the wrist position of the Phantom is used to command the wrist position of the excavator (the end of the stick), and the last degree of freedom of the gimbal is used to control the curl of the bucket. The Phantom command is given as a position $[x_p, y_p, z_p, \theta_p]$ and correlates to the position of the excavator wrist $[x_4, y_4, z_4]$ and the bucket angle θ_5, i.e. $[x_p, y_p, z_p, \theta_p]$ from the Phantom maps to $[x_4, y_4, z_4, \theta_5]$ as shown in Fig. 12.

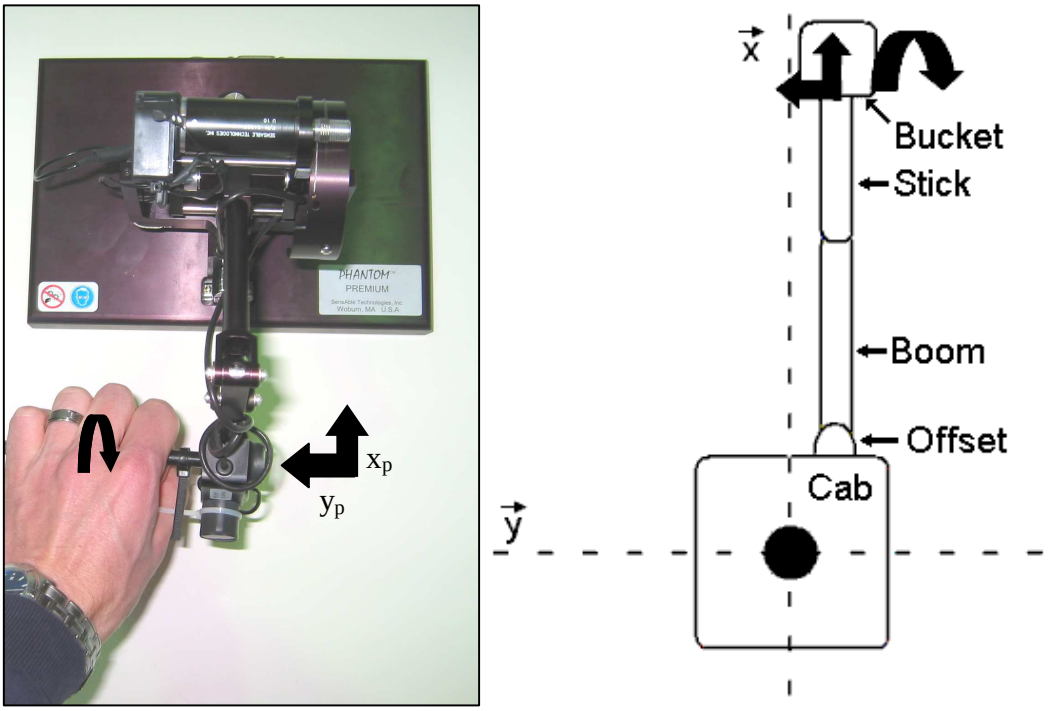

Fig. 12 Position Control Mode. The black arrows denote the position relationships between the controller and the excavator. The right hand figure is an overhead view of the excavator.

Hybrid Control Mode

For hybrid control, the position of the Phantom [x, y, z] gives the hybrid command of [r, $\dot{\theta}_1$, z]. The magnitude of the commanded y position is correlated to the commanded $\dot{\theta}_1$ by equations 86 and 87.

$$\text{if } |y_{command}| > \frac{1}{2} deadband \quad \dot{\theta}_1 = y_{command} - \frac{1}{2}(deadband) \cdot sign(y_{command}) \tag{86}$$

$$\text{if } |y_{command}| \leq \frac{1}{2} deadband \quad \dot{\theta}_1 = 0 \tag{87}$$

where *deadband* is a software implemented strip that gives a zero velocity command. The curl of the bucket relates to the position of the rotating handle, i.e. [x_p, y_p, z_p, θ_p] from the Phantom maps to [r_4, $\dot{\theta}_1$, z_4, θ_5] as shown in Fig. 13.

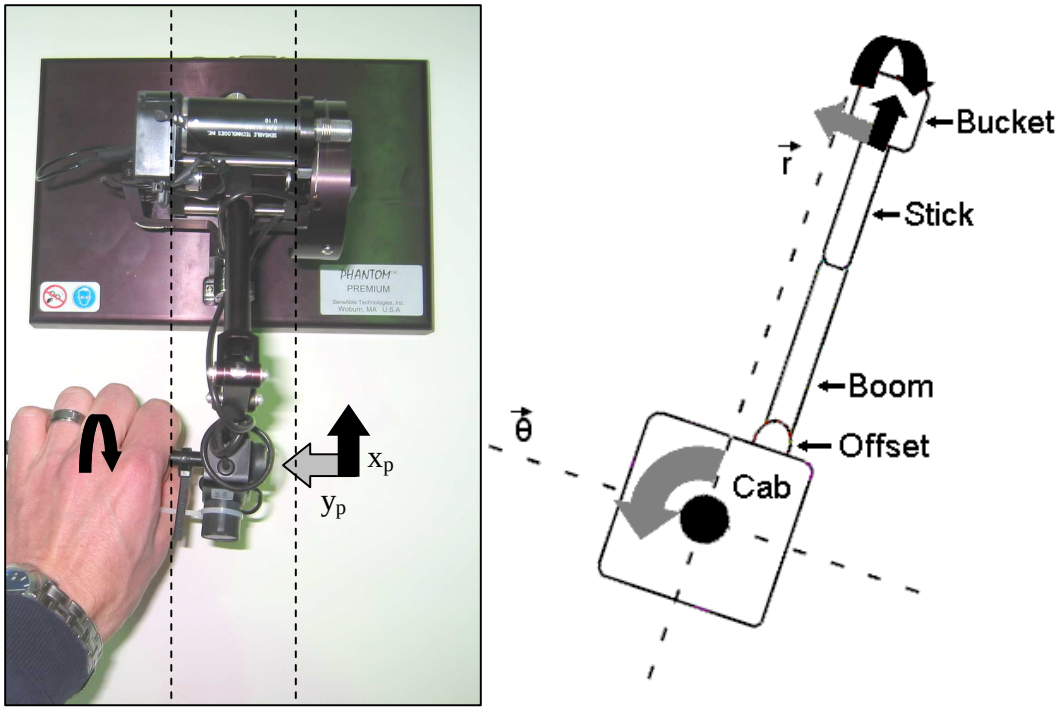

Fig. 13 Hybrid Control Mode. The black arrows denote the position relationships between the controller and the excavator. The gray arrows relate the left-right position of the controller to the velocity of the excavator. The velocity command can be pictured as the rotational velocity of the cab or as the velocity of the wrist in the rotating $\vec{\theta}$ direction and scaled according to the radial position of the wrist. The deadband is the area between the dashed lines in the photograph on the left.

Limiting Input

The Phantom device workspace is very small compared to the excavator workspace. The workspace of the Phantom is scaled so that it covers the entire front half of the workspace of the excavator (Fig. 14). This allows the operator to command positions outside the workspace, which must be converted to positions inside the workspace so that the transformation algorithms produce real and meaningful values and so that the machine works appropriately. The key parts of the input limiting algorithm is (1) to produce a smooth trajectory as constantly out-of-workspace commands are given and not to jump from one boundary point to another and (2) to create smooth transitions

as a commanded trajectory passes from an in-workspace command to an out-of-workspace command and vice versa.

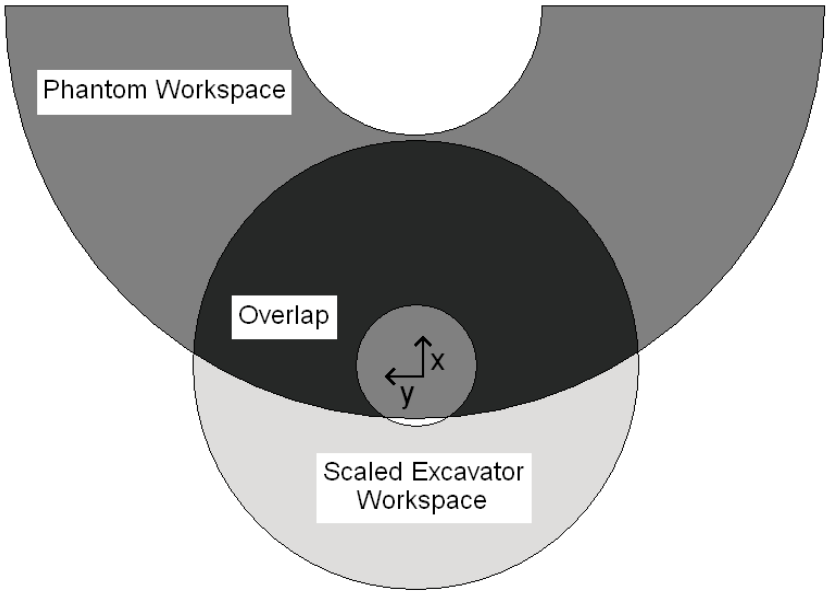

Fig. 14 Overlapping Workspaces for Position Control Mode. The figure shows a horizontal cross-section of the Phantom workspace and the scaled excavator workspace. Inner and outer diameters of both workspaces vary with height. The coordinate system shown is for the Phantom and the excavator with the z-axis coming out of the page.

The Bobcat 435 cab can rotate a full 360^{o}. In order to decrease the scaling factor, the swing of the simulated excavator is limited to $\pm 90^{o}$. The space behind the excavator is not of interest during HMI testing, but if the whole workspace is needed, the scaling factor can be increased so that the space behind the excavator lies within the workspace of the Phantom and the $\pm 90^{o}$ rotation limitation removed.

In the vertical plane, the commanded z position is not limited unless it is higher than the highest reachable spot (area 1 on Fig. 15) or lower than the lowest reachable spot (area 2 on Fig. 15). If the commanded position falls in area one, then the limiting

algorithm commands the highest point possible. If the commanded position falls in area two, then the limiting algorithm commands the lowest point possible.

If the commanded position falls in either area three or four, z_d is kept and the x_d:y_d ratio is maintained. The resulting commanded position is the closest point on the boundary of the workspace at the same commanded height.

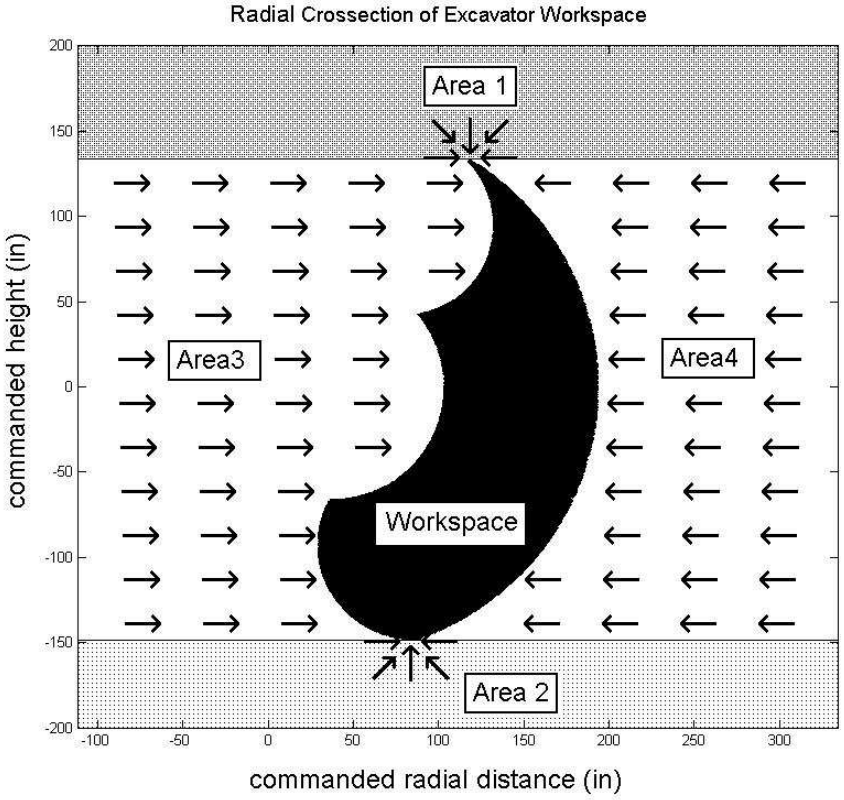

Fig. 15 Radial Cross-Section of the Excavator Workspace. With scaling this is also representative of a radial cross-section of the overlap in Fig. 14.

If the Phantom is used in hybrid mode ([r, $\dot{\theta}_1$, z]) the position scaling remains the same in the Phantom's x-z plane and the out-of-workspace locations are only in the Phantom's x-z plane (Fig. 16 – see Fig. 14 for the Phantom's coordinate frame).

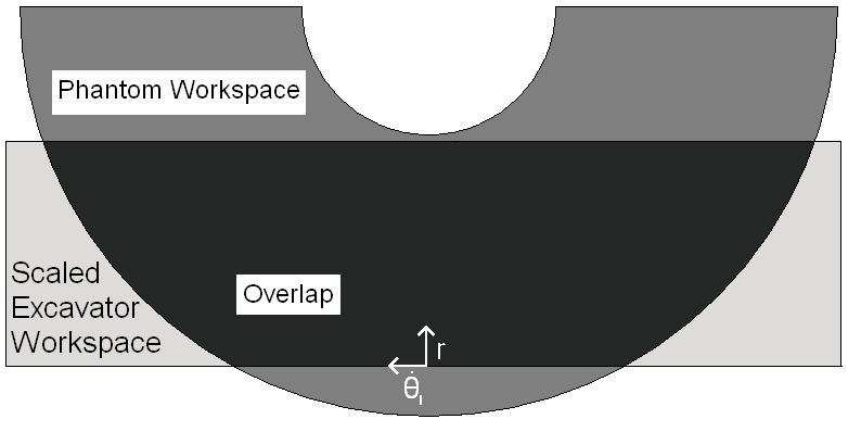

Fig. 16 Overlapping Workspaces for Hybrid Control Mode. The figure shows a horizontal cross-section of the Phantom workspace and the scaled excavator workspace. Inner and outer diameters of both workspaces vary with height. The coordinate system shown is for the excavator. The z-axis comes out of the page.

The out-of-workspace locations and are mapped back into the workspace in the same manner as in Fig. 15, except that the now Fig. 15 shows a vertical rather than radial cross-section of the scaled workspace. The $\dot{\theta}_1$-axis in Fig. 16 has no limitations.

Force Feedback Schemes

Four different force feedback schemes were developed: digging force reflection, workspace wall, virtual Phantom-excavator spring, and hop-on. None, any, or all schemes can be activated at any time. Only digging force reflection and hop-on were used for the testing.

Digging Force Reflection

The soil model calculates the force and moment from the environment at the excavator wrist and the environmental force at the tip of the bucket. These forces are combined and scaled and then fed back to the operator. In application this force would be measured with force sensors, calculated from hydraulic pressure, or inferred from other

measurements. The calculated force in the simulation is very uneven and can have a significant high frequency component to it (top graph in Fig. 17). The high frequency occurs when the bucket is in the soil and oscillating very quickly around the equilibrium point (the point where the forces applied to the soil by the bucket equal the forces applied to the bucket by the soil). The bucket is not moving quickly, so the damping component of the soil force is very small. In the new soil model developed in Chapter 3, the spring component of the soil force is dependent on the direction of the velocity, and the velocity is switching direction every one or two time steps (1 or 2ms). Therefore, the spring force changes magnitude by a factor of 10, but the direction does not change. In the upper graph in Fig. 17, the bucket reaches the equilibrium point around 2.5s. The force then switches back and forth so quickly that it appears as a thick solid line. The top of the line is around 7000 N and the bottom is around 700 N, the factor of 10 coming from the factor of 10 change in the spring constant. This chattering effect can be lessened by reducing the spring constant of the soil. For lower spring constants the chatter is still present but the cycle time is longer. For a spring constants ten times softer, the chatter is reduced to an oscillation of around 1000N and a period of 6-7ms.

The $sign(\dot{y}_k)$ is a possible source of chatter in equations 58 and 59. However, the F_{ck} term is small enough that the chattering it causes is small. If this term were to be the cause of the large magnitude chattering seen in Fig. 17, then chattering should be seen when the bucket velocity is near zero both in and out of the soil. When the bucket is out of the soil and the tip velocity is approximately zero, very small magnitude chattering takes place. The bucket tip position oscillates back and forth around zero every 1 to 2 time steps, but with an amplitude of .001 inches. These small oscillations could cause the

soil force calculations to change the spring constant back and forth by an order of magnitude. To test this, the F_{ck} term is set equal to zero for all actuators. The calculated force shows the same behavior – neither magnitude nor period of the oscillation changes. Hence, any small chattering effects caused by the $sign(\dot{y}_k)$ term in equations 58 and 59 do not cause the chattering shown in the soil model. The chattering in the soil model must arise from the sudden magnitude switch in k_n, k_t, and k_θ, in equations 65, 66, and 67.

The magnitude switching of k_n, k_t, and k_θ implemented in the *Small Bucket Retractions* section (pg. 35) is used to make the discrete time simulation of the excavator-soil interaction force produce a response in the excavator arm that is similar to the real world, continuous time response. The expected response in a continuous time system is that the bucket would penetrate the soil until it reaches an equilibrium point. There may be small oscillations in position around the equilibrium point and the applied soil force may oscillate quickly, or the force applied by the soil may be constant and the bucket will sit still at the equilibrium point. Regardless if there is a real world high frequency force oscillation or not, the force sensors, pressure sensors, or other means used in a real world system to measure the applied force, would not show a high frequency component.

The high frequency force causes the Phantom to buzz in the operator's hand. This buzzing is a meaningless signal since it does not reflect an expected real world response, so the force feedback signal passes through a lowpass filter with a cutoff frequency of 8Hz (bottom graph in Fig. 17). This still allows the operator to quickly feel changes in the force, but eliminates the unrealistic buzzing. It gives the operator a feel for the applied force at equilibrium, which better reflects what would be seen in the real, continuous time system.

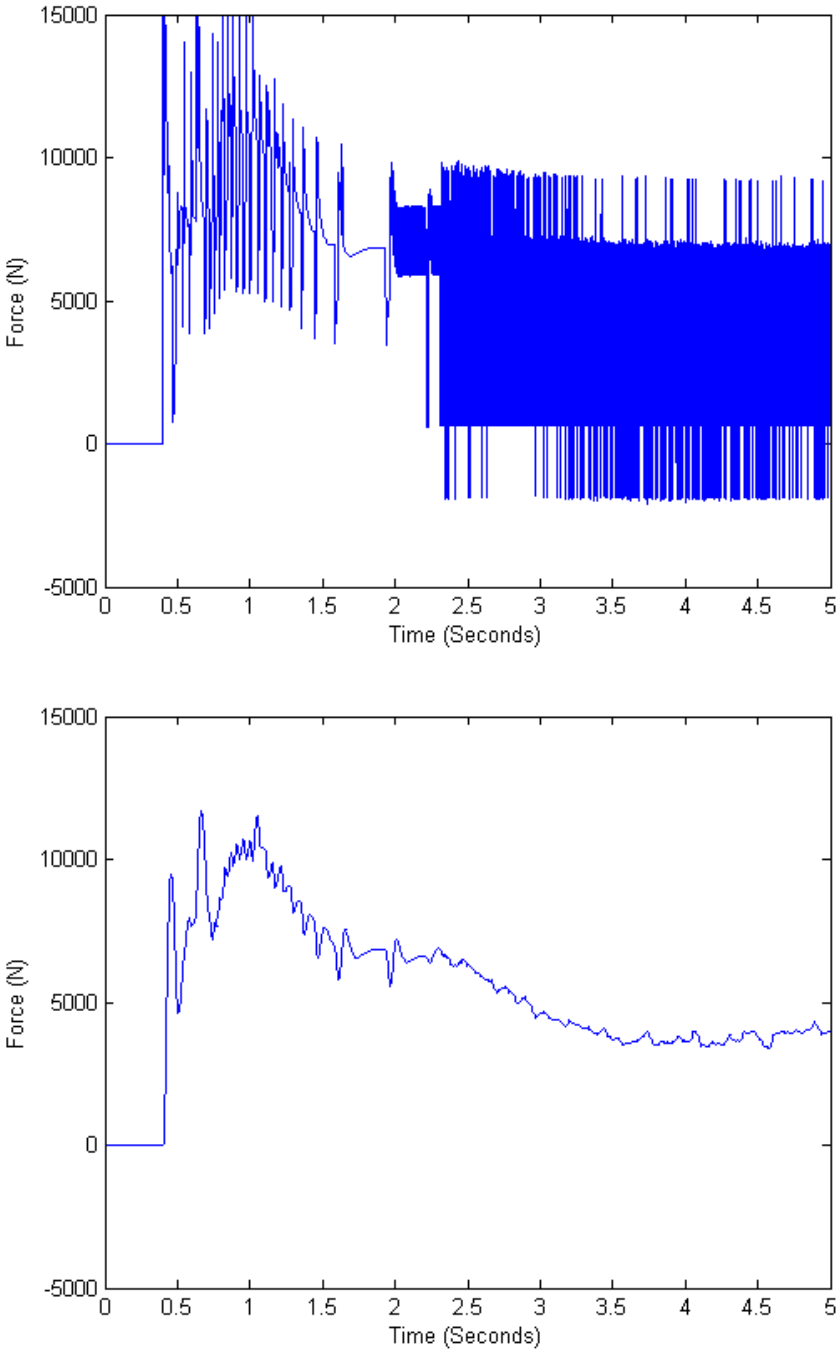

Fig. 17 Filtered and Unfiltered Digging Force Feedback Before Scaling.

Workspace Wall

The workspace of the Phantom is greater than the scaled workspace of the excavator (see Fig. 14). When the commanded position is outside the scaled workspace of the excavator then the commanded position is mapped back into the excavator workspace. To give the operator a feel of where the workspace boundaries are located, a force is applied whenever the commanded position is outside of the scaled workspace. This force is proportional to the displacement outside workspace.

$$f_w = k_w(x_d - x_a) \tag{88}$$

where f_w is the force of the haptic wall, k_w is the spring constant, x_d is the commanded wrist position, and x_a is the actual commanded wrist position mapped inside the workspace.

To avoid the rigid wall problem that causes chattering on the edge of the scaled excavator workspace, the force f_w is run through a lowpass filter, the same filter used for the digging force reflection (see Fig. 17). The effect is that the wall is spongier instead of being 100% rigid. However, it eliminates jerky forces at the limits of the workspace.

In position control mode, the workspace wall corresponds directly to the edges of the scaled excavator workspace in the Phantom workspace (Fig. 14). In hybrid control mode, the workspace wall is only applicable to the r and z directions, corresponding to the x and z directions of the Phantom (see Fig. 16). There is no wall force in the Phantom's y-direction.

Phantom-Excavator Spring

The operator can move the Phantom much faster than the excavator can respond. With position control, it can be difficult for the operator to tell where his command is in the workspace. Through visual feedback the operator knows the actual wrist position, and so a virtual spring is attached between the commanded wrist position and the excavator's wrist (Fig. 18). This force gives the operator a sense of where the commanded position is relative to the actual position of the excavator.

$$f_s = k_s(x_a - x) \tag{89}$$

where f_s is the force of the virtual spring, k_s is the spring constant, x is the excavator's wrist position, and x_a is the actual commanded wrist position. This force is only meant for use in position control mode and not in hybrid control mode.

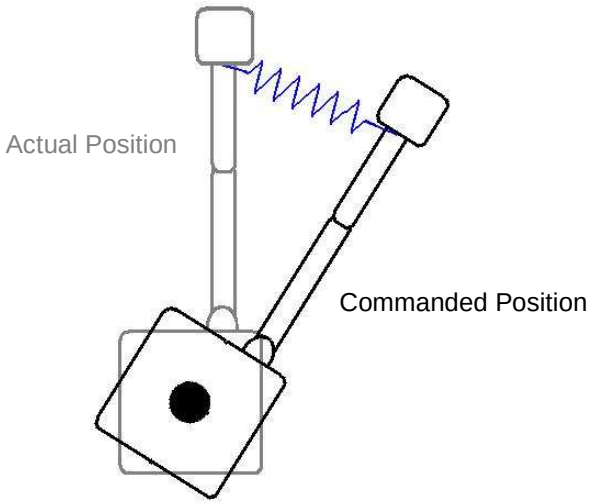

Fig. 18 Virtual Spring Feedback. The spring force is proportional to the distance between the actual and commanded excavator wrist positions. This is a bird's eye view of the excavator with the operator's head shown as a black circle.

Hop-on

The hop-on force is only used in hybrid control mode. A force proportional to the commanded velocity, but opposite in direction is fed back to the operator. This force allows the operator to sense the magnitude of the commanded velocity and where the edges of the deadband are located. It simply acts as a spring return for the y-axis of the Phantom (Fig. 19). The hop-on force, $f_{hop\text{-}on}$ is calculated by

$$f_{hop-on} = k_{hop-on}\dot{\theta}_1$$

where $k_{hop\text{-}on}$ is the spring force constant, and $\dot{\theta}_1$, the desired swing velocity, is calculated according to equations 86 and 87.

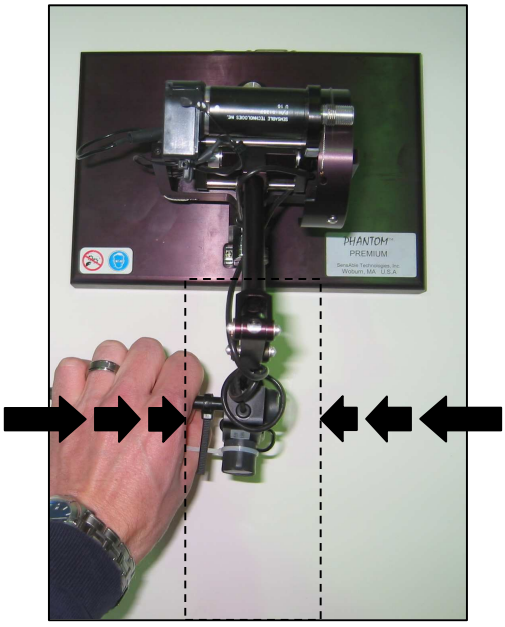

Fig. 19 Hop-on Force. The deadband outlined by dashed lines. The arrows show the hop-on force vector field.

Pump Control

The basic physical quantity being controlled is the displacement of each pump. Since the pumps' rotational speed is constant, the swashplate displacement and pump flow, Q, are proportional. A simple PD controller is implemented to calculate the desired pump flow, Q_d, based on the cylinder positions and velocities (Fig. 20).

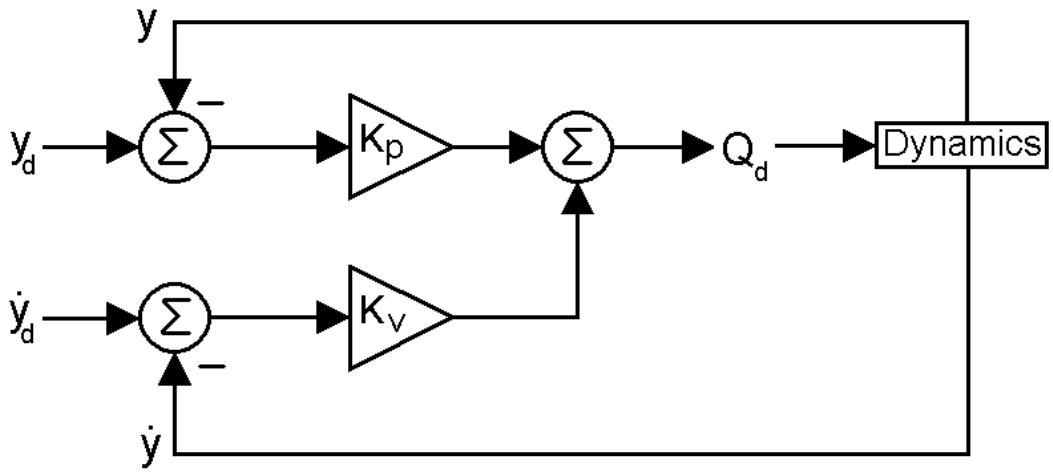

Fig. 20 Pump Flow Control.

CHAPTER 5

TESTING AND EVALUATION

Operator Work Station

The operator work station is the cab of a 435 Bobcat excavator (Fig. 21). The operator sits in the seat and controls the excavator using the Phantom that is mounted in front of him (Fig. 22 - 23). None of the excavator's hardware moves during the simulation, but the cab is in place to give the operator a more realistic feel.

On the windshield of the cab, a 52" LCD TV is mounted, covering both the upper and lower windshields. The TV displays the simulated excavator arm that the operator is controlling.

Fig. 21 Operator Workstation.

Fig. 22 Operator Sitting in the Cab. The operator is gripping the Phantom with his right hand.

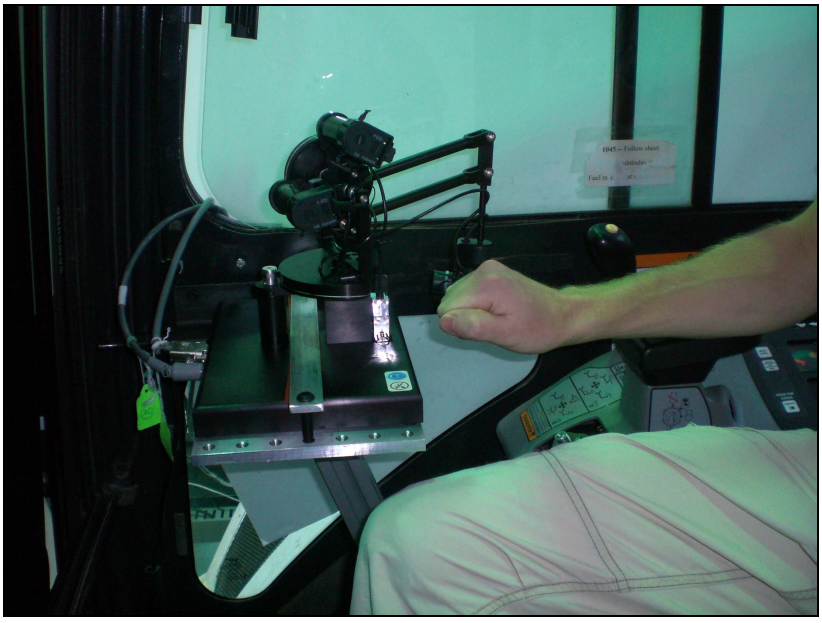

Fig. 23 Phantom Mounted in the Cab. The Phantom was mounted so that operators could use the stock excavator armrest to support their forearms.

Graphical Interface

The graphics of the simulated arm are drawn onto the TV screen by a program written for this thesis in C++ that uses the OpenGL library. The CAD models of the offset, boom, stick, and bucket links are reformatted as header files for the program. The cab is not shown since the operator is sitting in the actual cab. A variety of shareware 3D tree drawings found on the internet are transformed using Okino NuGraf and displayed to add a sense of depth to the flat ground (Fig. 24). However, the trees do not add adequate depth to the simulator, so shadows of the links are drawn on the ground. Since the OpenGL header files for each of the links contain tens of thousands of triangles and the shadowing algorithm requires a long series of math operations for each triangle, simplified files with less than fifty triangles are used to calculate the shadow of each link. The simplified links are not shown; they are only used for drawing the shadows.

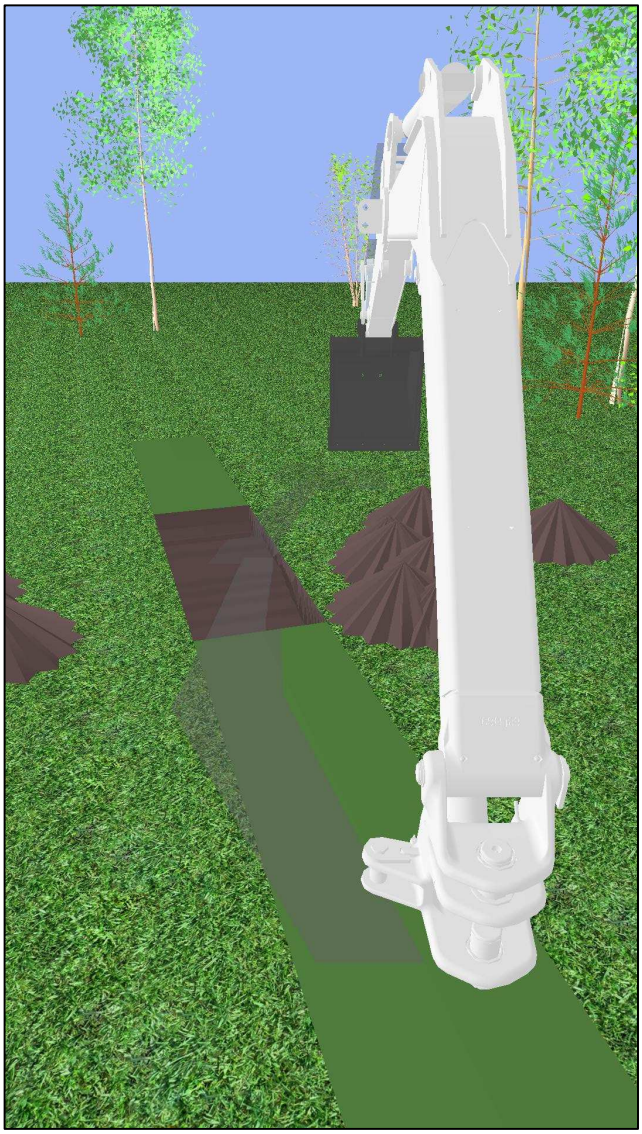

Fig. 24 Simulator Screenshot.

The desired trench is shown as a flat green rectangle drawn on the ground where the operator should excavate. The soil surrounding the trench has a grass texture applied to it so that it is easily differentiated from the green of the trench. The trench is divided evenly into 256 sections. Each section's dimensions are: the set trench width (roughly 1.2 times the width of the bucket), 1/256 of the trench length, and a depth determined by how much soil the operator displaces. The walls of the trench are drawn vertically, and the

floor of the trench is drawn by a series of rectangles connecting the different depths and tied to the walls of the trench (i.e. the four vertices are at the points (right wall, $depth_n$), (left wall, $depth_n$), (right wall, $depth_{n+1}$), (left wall, $depth_{n+1}$) See Fig. 25). If the soil in the trench is at the original level, it is colored green, but if not, it is colored brown.

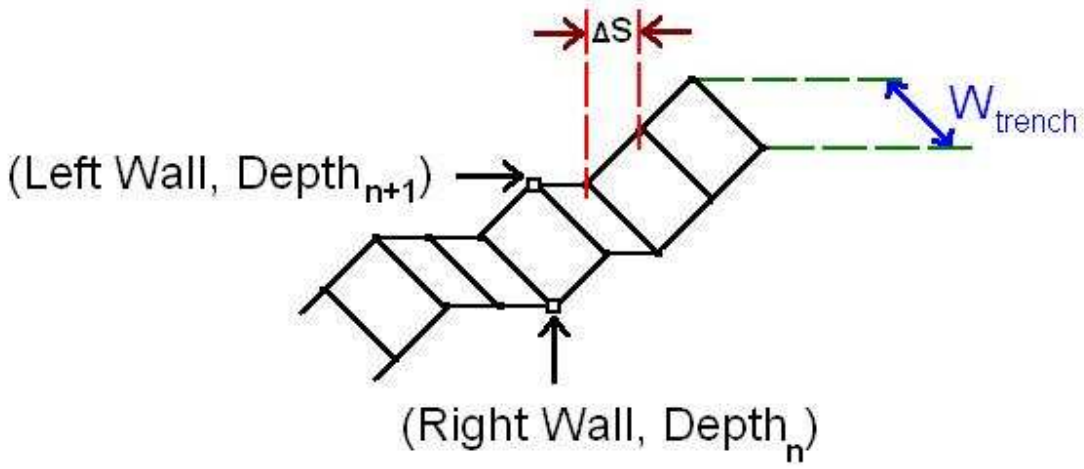

Fig. 25 Trench Floor Cutaway.

The soil in the bucket is displayed as a curved brown surface in the bucket. The height of the soil in the bucket is dependent on the calculated amount of soil in the bucket. There are a discrete number of heights available, so small changes in the amount of soil in the bucket do not necessarily produce a change in the display; however, it is also difficult for the operator to pick up only a small amount of soil.

When the soil is dumped, the visualization shows the bucket empty and draws a large number of small soil particles falling. The x and y positions of the particles are randomly obtained inside the area of the bucket. t is the time since the soil was dumped, which is determined by when the front face of the bucket passes the vertical. The z

position of the particles is calculated as $z_o + 1/2gt^2 \pm \delta$, where δ is a random number obtained for each particle and is less than the variation in x and y. The number of falling particles is proportional to the amount of soil in the bucket.

When $z_o + 1/2gt^2$ becomes less than the level of the ground, a pile appears. The piles are drawn as brown ridged cones, and are centered on the center point of the bucket at the time the soil is dumped. The angle of repose of the soil is set to be 45^o, so the radius and height of the pile are equal, and are calculated from the volume of soil in the bucket, V_{load}, as

$$r = h = \sqrt[3]{\frac{3V_{load}}{\pi}} \tag{90}$$

The program stores the location and volume of up to 100 piles. When the 101st load is dumped, the 101st piles appears the first pile disappears, when the 102nd load is dumped, the 102nd pile appears and the second piles disappears, and so on. None of the simulations require the operator to make more than 50 piles, so this unrealistic feature does not affect the realistic feel of the simulation. The piles may overlap unless the dirt is dumped with 8" of another pile. If so, the volume of the first pile becomes the combined volume of the first and second piles. If the volumes are not combined, the piles are so close to each other that they look like one pile, and it appears that even though the bucket dumped its load, a pile did not form.

If the soil is dumped back into the trench, the section of the trench that contains the same horizontal point as the center of the bucket receives 3% of the dirt. The remaining dirt is distributed over 50 points, 25 on each side of the center point.

The addition to each depth is calculated as

$$\Delta Depth = \frac{1-.03}{2}\left(\frac{50}{2}\right) + .001 \cdot (13-k)\left(\frac{V_{load}}{A}\right) \tag{91}$$

This creates a sloping two dimension pile inside the trench. 'A' is the area of one section of the trench, and k is the number of sections between the current trench section and the center section. As mentioned, $-25 \leq k \leq 25$.

Sound

The sound of the engine is played by two speakers in the cab to further immerse the operator in the virtual environment. A five second clip of engine noise is looped to play continually during the simulation. The volume is varied as a function of the hydraulic power required. The power each pump requires is calculated by

$$Power = P \cdot Q \tag{92}$$

The power needed by all four pumps is then summed together to get $P_{required}$. If the resulting power is greater than the power output by the engine at an idle (P_{idle}) then k becomes a positive constant, otherwise k = 0 in equation 93.

$$Volume = Volume_{idle} + k(P_{required} - P_{idle}) \tag{93}$$

This variation in volume is an important feedback cue used by excavator operators while digging as a metric for machine effort.

Network

The excavator simulator uses three separate desktop computers (Fig. 26). The excavator dynamics are calculated using Mathwork's Real Time Workshop on a PC running the xPC Target OS. This *XPC* machine solves the dynamics of the excavator's hydraulic and mechanical systems. The *Main PC* is used to compile the Simulink model

and load it on to the *XPC* machine. The *Main PC* also draws the graphical simulator, plays audio, and stores data. A third machine, the *Phantom PC*, interfaces with the Phantom and sends the commanded position and velocity to the *XPC* target machine. The computers are all connected via Ethernet cards to a small hub.

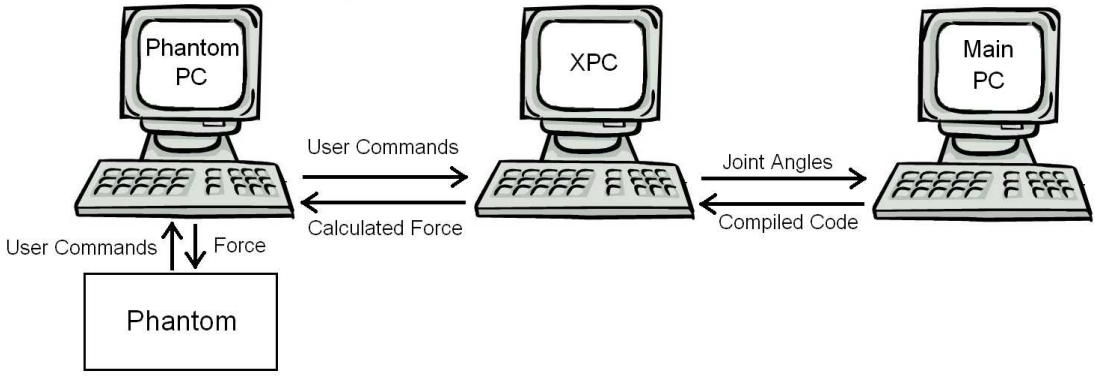

Fig. 26 Simulation Network.

The *Phantom PC* is a Dell desktop with a 1.7GHz processor and 512MB of RAM running Windows XP. The *XPC* machine is a Gateway 2000 desktop with a 333 MHz processor and 64MB of RAM. The *Main PC* is a custom desktop with a 2.4GHz processor and 2GB of RAM.

Human Factors Testing

To evaluate the possibilities of increasing machine efficiency and operator effectiveness, six individuals operated the simulated excavator with each of the new control interfaces. Six subjects from the Georgia Tech Intelligent Machine Dynamics Lab (IMDL) volunteered for the initial testing. This preliminary testing was not designed to produce statistically conclusive results, but to prove the viability of performing future conclusive tests and to show the viability of the tested control schemes.

Testing Procedure

The participants were each assigned a number and asked to fill out a pre-test questionnaire (Appendix A). The subjects were all graduate students and members of the IMDL, and as such, were familiar with the project's goals. The pre-test questionnaire gathered data about the subjects past experience with excavators and haptic joysticks (Fig. 27 - 30)

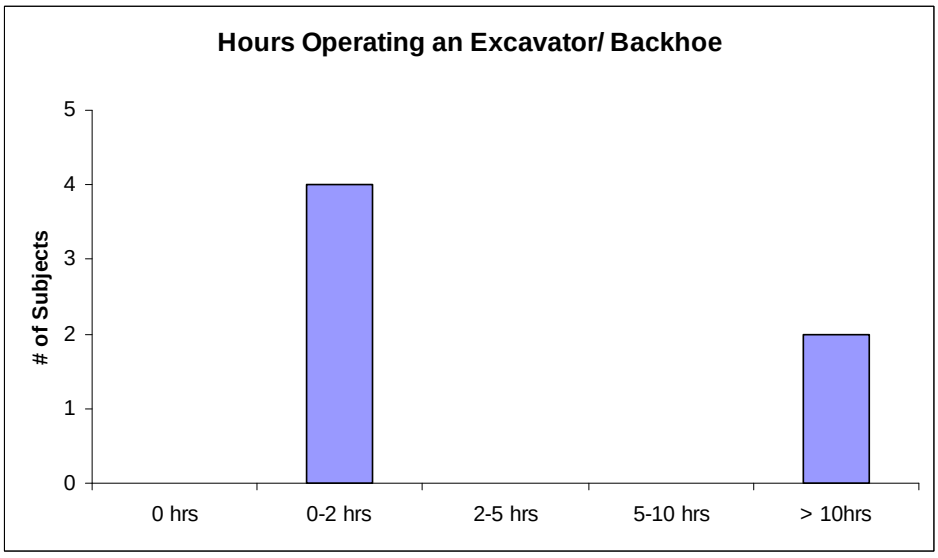

Fig. 27 Subjects' Past Experience with Operating Excavators and Backhoes. None of the subjects were experience operators.

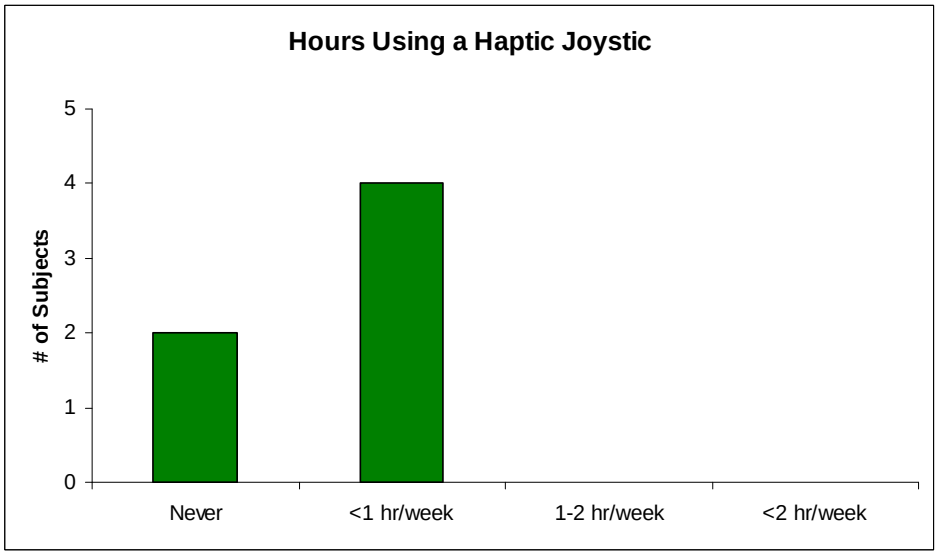

Fig. 28 Subjects' Current Haptic Joystick Use. The IMDL has multiple projects involving haptic feedback, which several of the subjects work on directly.

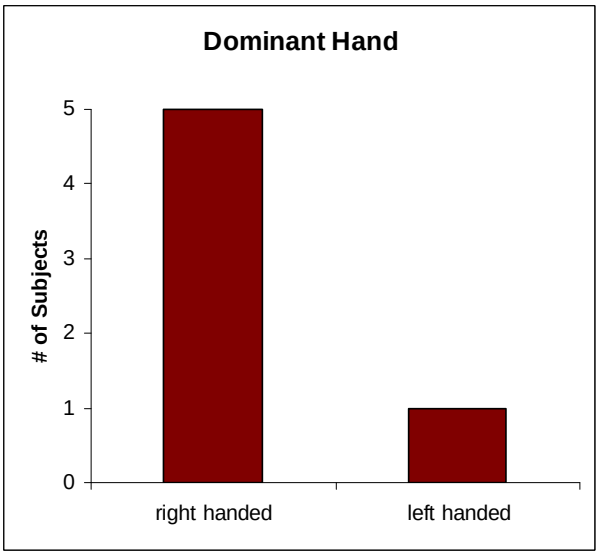

Fig. 29 Subjects' Dominant Hand. One of the subjects was left-handed. The Phantom is currently only capable of being mounted on the right hand side of the cab, so the left handed operator used his right hand to move the Phantom. To see how this may have affected performance, see the data plots in Appendix B: Subject 6 was the left handed operator.

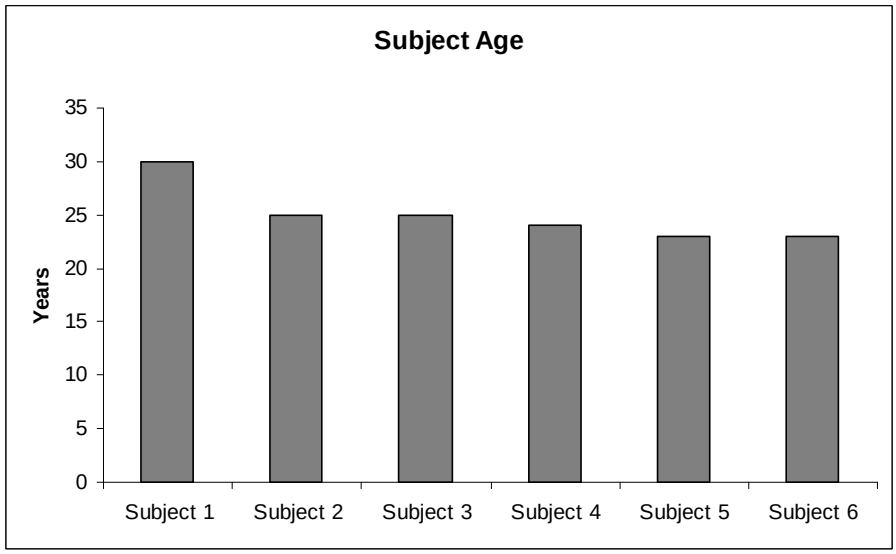

Fig. 30 Subjects' Age. The subjects were not purposefully tested in age-descending order.

After completing the questionnaire, the subjects were told about how the simulation works and informed about anomalies such as not being able to move the dirt outside the trench but still being able to penetrate the soil. The position and hybrid controllers were explained and then the subject was able to use each controller for two minutes to see the difference. The hop-on force was activated for the hybrid control during the two minute session and was always present during the testing whenever hybrid control mode was used. Digging force feedback was explained and then the subject was given two minutes with each controller (position and hybrid) with the digging force feedback enabled.

The subject was then given one primary goal and two secondary goals:

- remove as much dirt as possible from the trench (primary goal)
- place dumped dirt in a large pile (i.e. dump each load as close as possible to the previous ones)
- Enter the trench without contacting the soil outside the trench.

The subjects were then given two minutes to accomplish the goals with each controller with and without haptics. Each of the possible scenarios below was repeated twice in a different order for each subject.

a) Position control

b) Hybrid control

c) Position control with force feedback (digging force reflection enabled)

d) Hybrid control with force feedback

After all eight trials the subjects filled out the post-test questionnaire (Appendix A).

During the tests, several different measurements were recorded. To evaluate the first goal, the volume of dirt removed from the trench was measured. To evaluate the second goal, the dumping locations were recorded and evaluated for proximity. To evaluate the third goal, the number of soil-strikes outside the trench and the number of times the bucket entered the trench were recorded. In order to evaluate machine efficiency, the pump flows and workport pressures were multiplied together to find the total energy used.

Human Factors Testing Results

The small number of subjects and the small group of people that the subjects were selected from, along with the simplicity of the tests and analysis, do not allow for statistically significant results. The results do show that the testbed allows performance improvements to be measured for human-machine interfaces – improvements that could not before be measured. The simulated excavator also needs to be compared to the actual

machine to verify that the model behaves realistically, before these testing results can be considered as valid.

The data for both runs for each subject with each control scheme were averaged together to give an overall score for each measurement with each control scheme for each subject, for example, Fig 31.

The primary goal was to remove as much dirt from the trench as possible. The total amount of soil removed during the run was recorded in cubic yards. To determine how close the piles were placed, the standard deviation of pile positions was taken and used as the metric for comparing pile proximity. To determine trench hitting accuracy, the number of times the operator entered the trench without hitting the soil outside the trench was divided by the number of times the operator entered the soil, whether inside or outside the trench. Energy efficiency was determined by dividing the amount of soil removed in the trial by the total amount of energy used by all four pumps during the trial. The result was measured in joules/cubic yard.

The operators' performance on each of the given three goals was quite different. Some operators achieved certain goals better on a certain controller and others did much better on other controllers. For example, the primary goal of removing as much soil as possible from the trench was best achieved by half of the subjects using position control with force feedback (Fig. 31). Of the other three subjects, each did better with a different one of the remaining three control schemes.

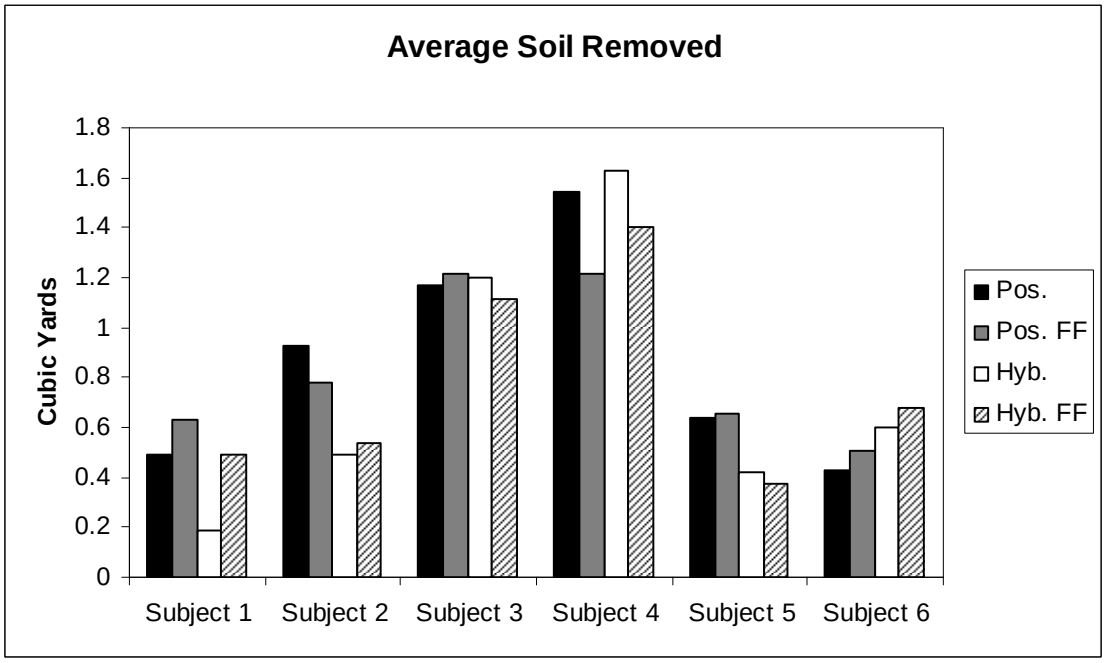

Fig. 31 Subjects' Average Soil Removed From the Trench. There is not a clear 'better' controller for removing soil from the trench.

However, with some measurements, such as the standard deviation in dump pile positions, there were clear improvements (Fig. 32).

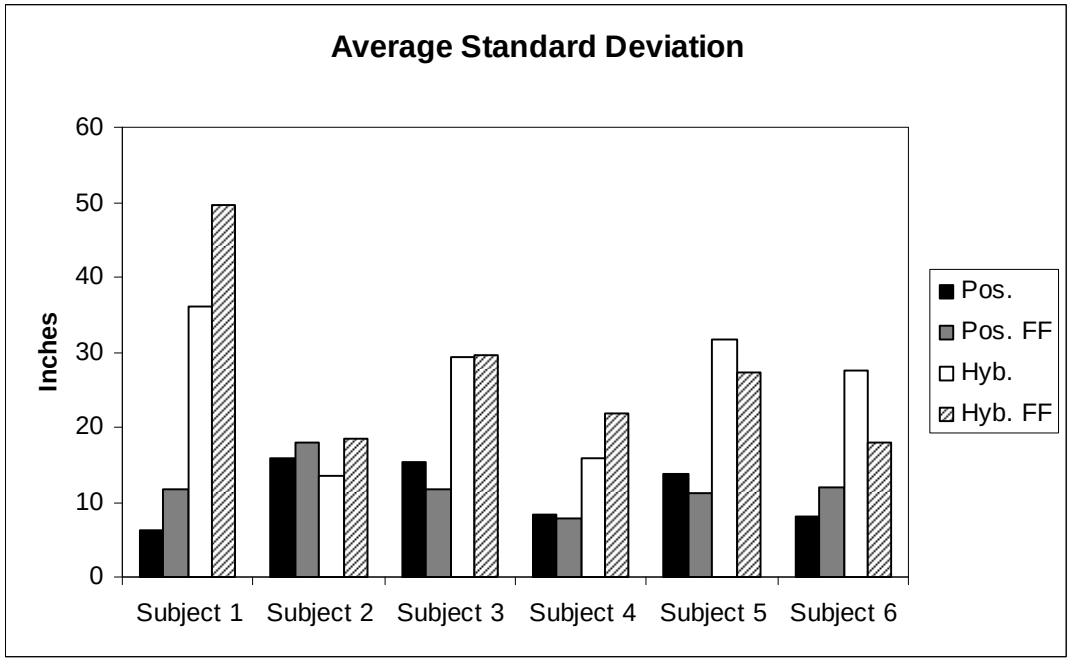

Fig. 32 Subjects' Average Standard Deviation of Pile Spacing.

The average standard deviation in 5 of the 6 cases is less with the position controllers than with the hybrid controllers.

The data for each goal was normalized by the position control scheme data for that goal to bring out relative improvements. Although the subjects were not told explicitly to be energy-conscious, the amount of energy required to remove a cubic yard of dirt was calculated for each control scheme (Fig. 33).

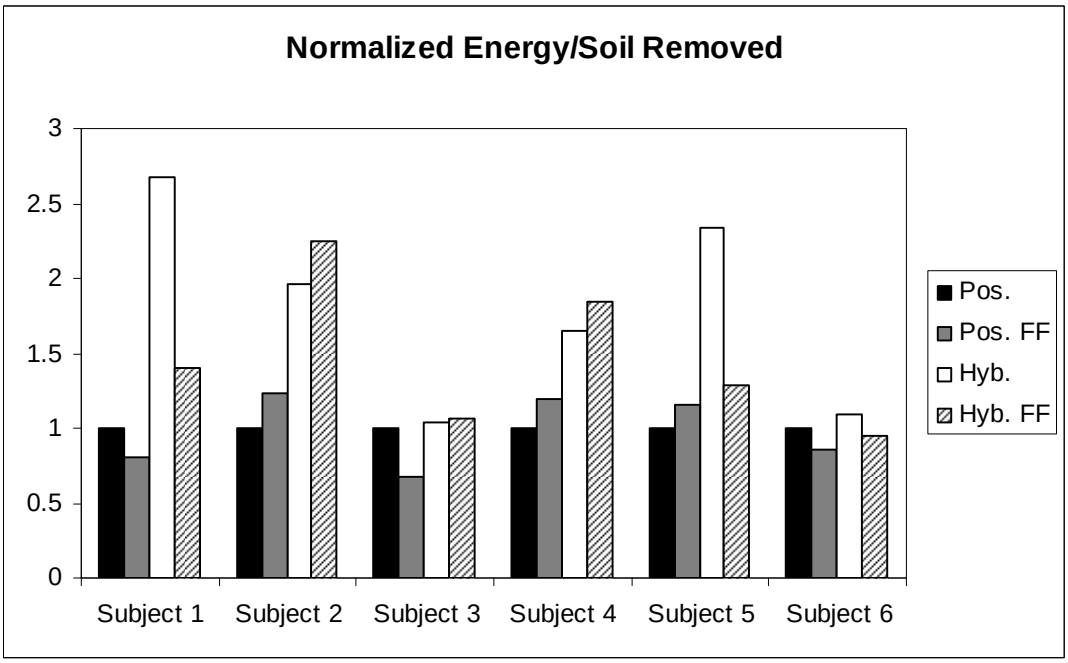

Fig. 33 Subjects' Normalized Energy/Soil Removed Rankings. The position controllers showed a clear lead in energy efficiency.

The normalized values for each of the control schemes were averaged for all the subjects. A pile proximity measurement was created by inverting the standard deviation (since low standard deviation in pile placement corresponds to better performance.)

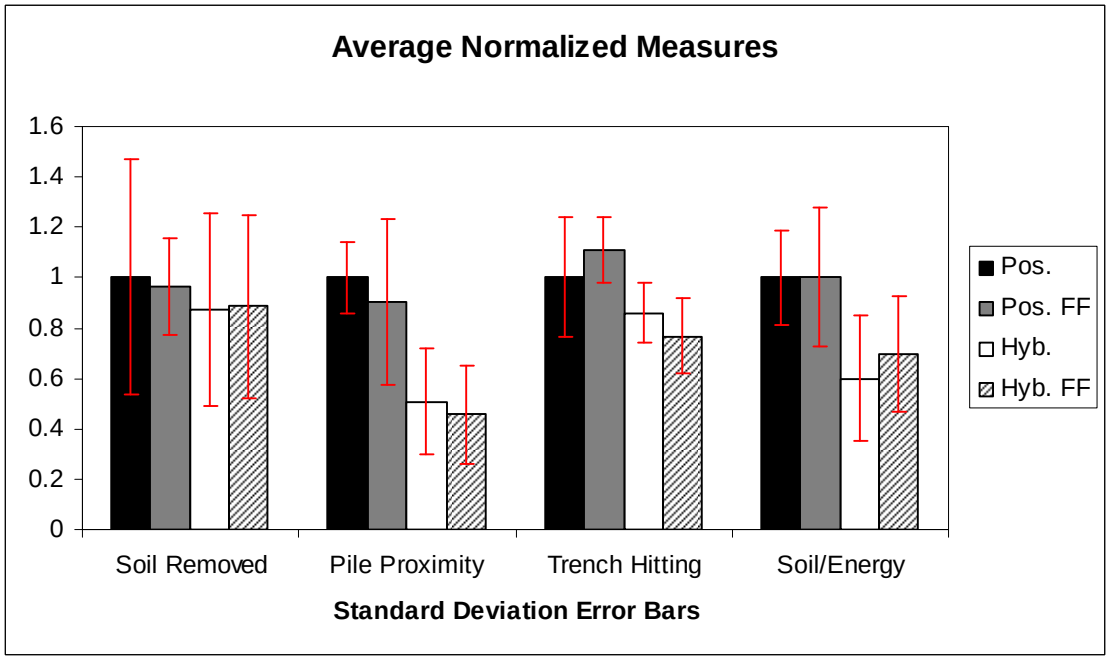

Fig. 34 Overall Rankings. The average with standard deviation bars for all test subjects normalized with respect to position control mode.

The results show that the position controllers did better in all aspects (Fig 34). However the standard deviation (shown by the error bars) is quite large. This is expected since a brief look at the data shows large variances from subject to subject (see Appendix B for all data plots).

Learning

Since the subjects had very short experience with the excavator simulator (eight minutes total), learning could play a large role in how well the subjects did with each control scheme. In other words, the subjects might do better with the control schemes that they used last, not because the control scheme was better, but because they had learned how to better manipulate the simulation. For example, they could have learned how to better hold the device so that was easier to control or didn't shake as much.

As an indicator of the role learning played in the operators' performance, the results were plotted against time. Each plot was examined for either continually increasing or decreasing values. None were found. Subjects 5 and 6 showed generally increasing or decreasing data for certain measurements (for example, Fig. 35). A best-fit line was put on the data since it appeared to be roughly linear. In Fig 35, the figure containing the most linear time-dependant relations, the R^2 values for Subject 5's and Subject 6's data are 0.83 and 0.67 respectively, demonstrating a fairly linear relationship and a possibility of learning effects. However, for the other four subjects, the R^2 values are 0.27, 0.19, 0.14, and 0.06, showing a minimal relationship. The best fit lines for some of the subjects have a negative slope, which strongly suggest that learning was not occurring.

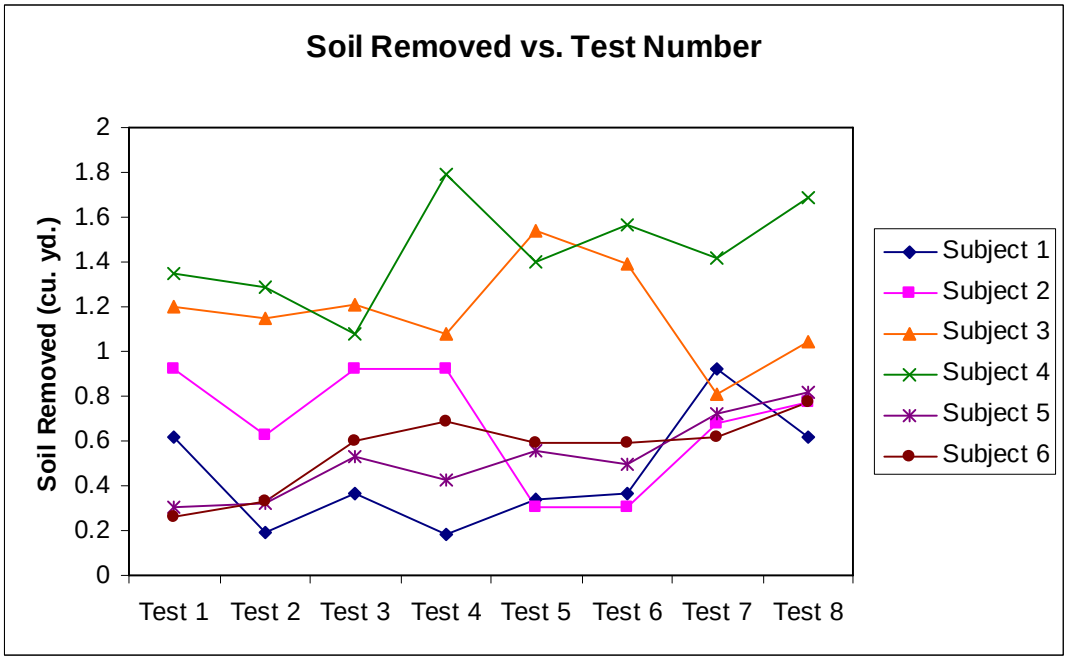

Fig. 35 Minimal Learning Is Seen. There is a lack of constant increase in the amount of soil removed from the trench as the tests continue.

To further investigate the possible effects of learning, the percent increase of the second test run compared to the first test run were plotted for the four performance measures for each subject with each control scheme (Fig. 36 - 39).

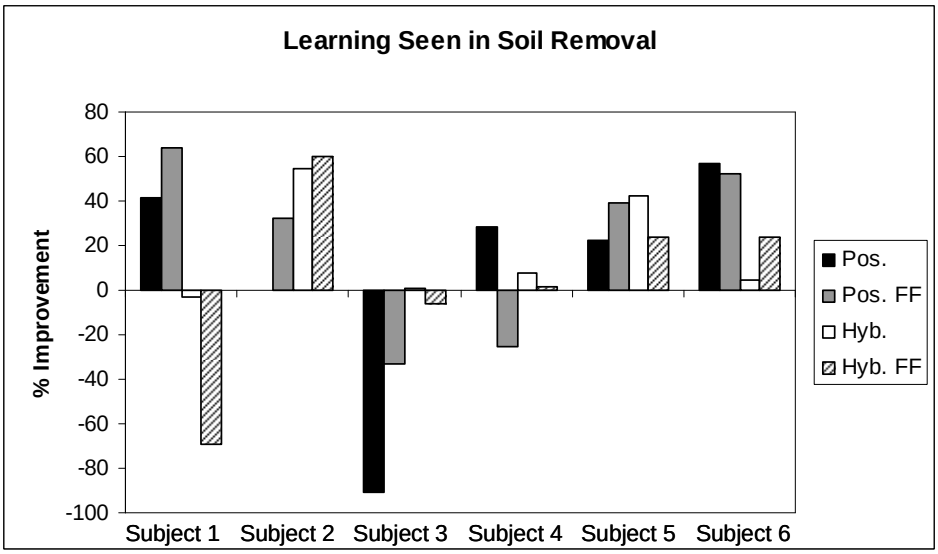

Fig. 36 Learning Effects in Soil Removal. Subjects 5 and 6 show increases for every control scheme. Learning possibly played a large role with these subjects and Subject 2.

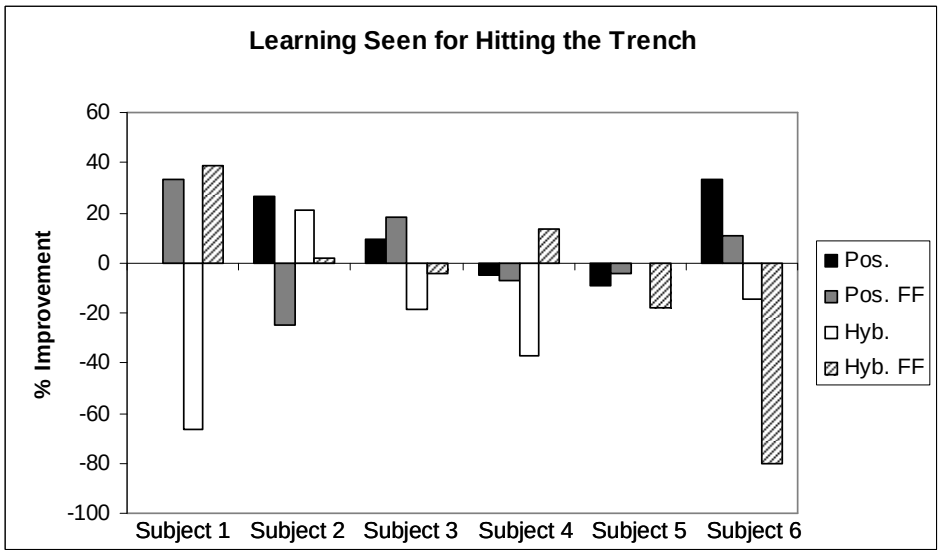

Fig. 37 Learning Effects for Trench Hitting. None of the subjects showed significant learning for more than two of the control schemes.

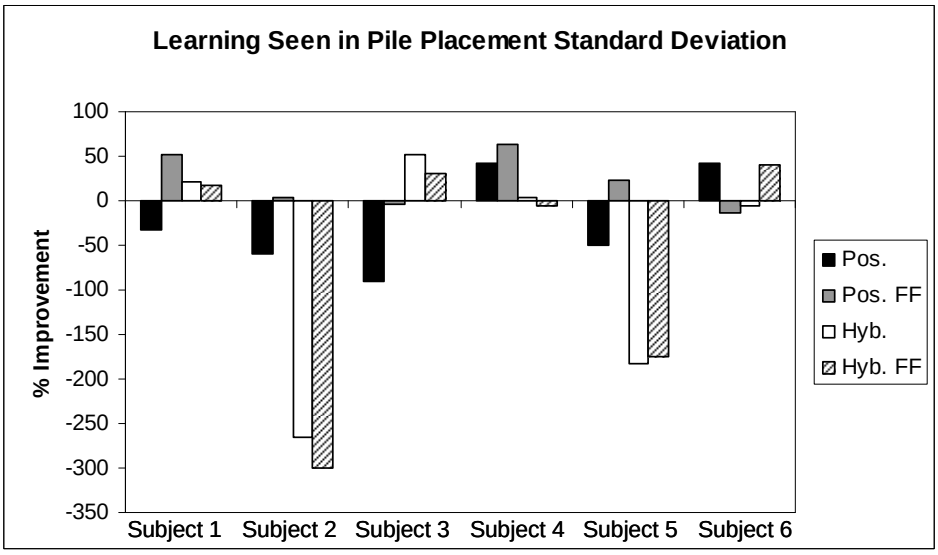

Fig. 38 Learning Effects for Pile Placement. None of the subjects showed significant learning for all of the control schemes.

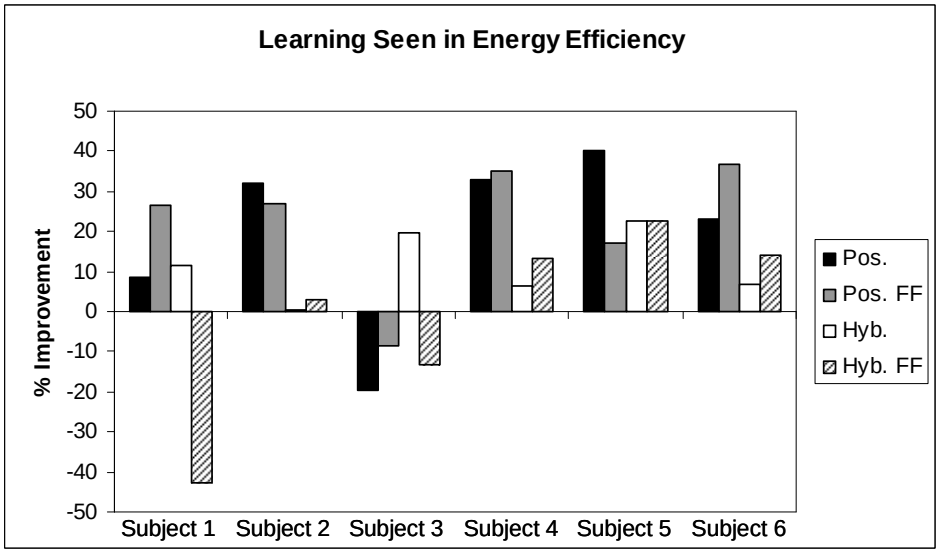

Fig. 39 Learning Effects for Energy Efficiency. The subjects were not told to be energy efficient, but subjects 4, 5, and 6 all show performance increases for all four control schemes.

The lack of general upward trends in Fig. 35 suggests that the learning curve is shallow enough after the first four trials that improvements arising from the operators' learning were negligible, and therefore changes are more dependent on changing the control scheme than on learning. However, for some measures, such as soil removal, certain subjects (in the case of soil removal, subjects 2, 5, and 6 – see Fig. 36), show the

possibility of having significant learning effects. The learning effects would need to better calculated and subtracted out in further and more conclusive tests.

Operator Observations

The subjects were asked to rank the controllers after the testing was over. They were to rank the controllers from 1 to 4 (with 4 being the best) for five criteria: easiest to learn, allowed you to dig the fastest, easiest to use, gave you the most accurate tip position, and which controller you prefer the most.

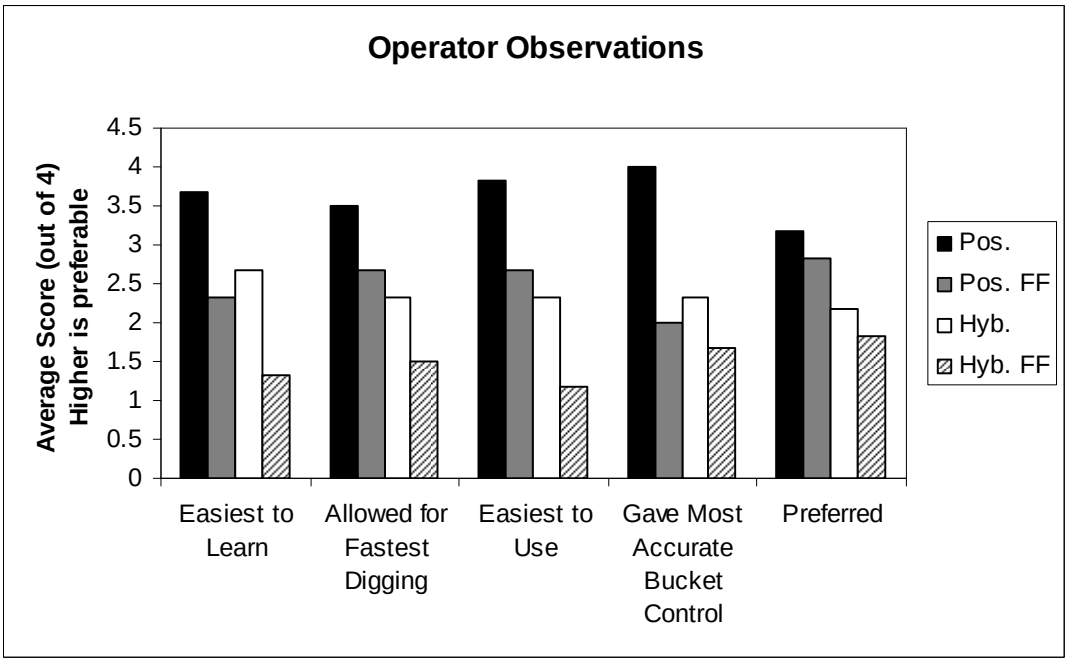

Fig. 40 Operator Preferences. Position control was the clear winner in all categories.

The operators selected the position controller as "best" in all categories and hybrid control with force feedback as the "worst" in all categories (Fig. 40). The subjects' observations correlated fairly well with the measured data. The subjects' thought they could dig the fastest with the position controller, and they were indeed fastest with the position controller (see Fig. 34). The subjects also thought that the position controller

allowed for the most accurate tip control, but they were better at hitting the trench with position control with force feedback.

The operators were asked what improvements could me made. Many responded that the force was too great and one even said the Phantom was ripped out of his hand. The force never exceeded 5N but was very jerky even after being filtered. It is the author's opinion that the jerkiness of the Phantom results in it being difficult to control, rather than the actual magnitude of the force feedback. The workspace of the Phantom is so small compared to the workspace of the excavator that the forces applied to the Phantom can cause small movements of the operator's hand, and these small hand motions command much larger motions of the excavator. This may cause the tip of the excavator to either move into an area of no force, or even opposing force. For example, if the bucket is moving forward through the soil and the jerkiness of the reflected digging force pushes the operator's hand backwards, the operator may command the bucket to go backwards. When the bucket retreats backwards, the back of the bucket comes in contact with the ground and the reflected force then pushes the operator's hand forward. This can lead to an oscillatory cycle until the operator changes his hand's stiffness or damping.

Other improvements suggested by the test subjects included:

- Reducing the force
- Improving the bucket handle to have hard stops and be easier to hold
- Separate the bucket control from the wrist position control
- Provide a counterweight to the Phantom so that it's "weightless"
- Reduce controller sensitivity (this could be improved by changing the excavator:Phantom workspace ratio)
- Reposition the armrest
- Improve system response time

CHAPTER 6

CONCLUSION

Contributions

This work's main contribution is the development of a real-time excavator simulator with a realistic display and accurate dynamic models of the excavator's hydraulic and mechanical systems and of the soil. The hydraulic system model consists of variable displacement pumps for control rather than the standard valves. A novel soil model is developed upon previous work to meet the need of real-time discrete simulations. The graphics program has a larger degree of realism than other academic simulators because it includes actual CAD models of the excavator links, shadows, plants, and falling dirt [28]. An operator work station was created with a stock Bobcat 435 cab for added realism.

A Phantom joystick was mounted inside the work station. Several force feedback schemes and two different coordinated control schemes were developed. From these, four different overall control schemes were selected and proof of concept testing was done to determine if appropriate tests could be done to evaluate multi-modal controllers with respect to operator effectiveness and machine efficiency. The simulator construction allows new human-machine interfaces to be tested for potential increases in operator effectiveness.

Recommendations for Future Work

Immediate future work should include making the small changes suggested by the test subjects. In particular, changes should be made to the digging force reflection to make it smoother. The development of this test stand allows for easy testing of new human-machine interfaces. Other coordinated control schemes combined with different haptic feedback schemes should be developed and evaluated. Those that give promising results with a small test group could be tested on a larger scale to give statistical validity. The stock valve controlled excavator could be modeled and used as benchmark for the larger scale tests.

APPENDIX A

TESTING QUESTIONNAIRES

PRE-TEST QUESTIONNAIRE SUBJECT # ___

How many hours have you operated an excavator or backhoe?

1) 0 hrs
2) 0-2 hrs
3) 2-5 hrs
4) 5-10 hrs
5) >10 hrs

Are you **left** or **right** handed? (circle one)

How regularly do use a haptic joystick?

1) Never
2) <1 hr/week
3) 1-2 hrs/week
4) >2 hrs/week

Age__

POST-TEST QUESTIONAIRE SUBJECT # ___

Rank the following from 1 – 4 where 4 is the control that most identifies with the phrase above

Which of the control schemes was easiest to learn?

__ Hybrid control
__ Position control
__ Hybrid control with haptics
__ Position control with haptics

Which of the control schemes allowed you to dig the fastest?

__ Hybrid control
__ Position control
__ Hybrid control with haptics
__ Position control with haptics

Which of the control schemes was easiest to use?

__ Hybrid control
__ Position control
__ Hybrid control with haptics
__ Position control with haptics

Which of the control schemes allowed you to most accurately control the bucket position?

__ Hybrid control
__ Position control
__ Hybrid control with haptics
__ Position control with haptics

Which of the control schemes do you most prefer?

__ Hybrid control
__ Position control
__ Hybrid control with haptics
__ Position control with haptics

How would you suggest improving the ergonomics of the joystick/armrest?

What other improvements could be made?

APPENDIX B

DATA PLOTS

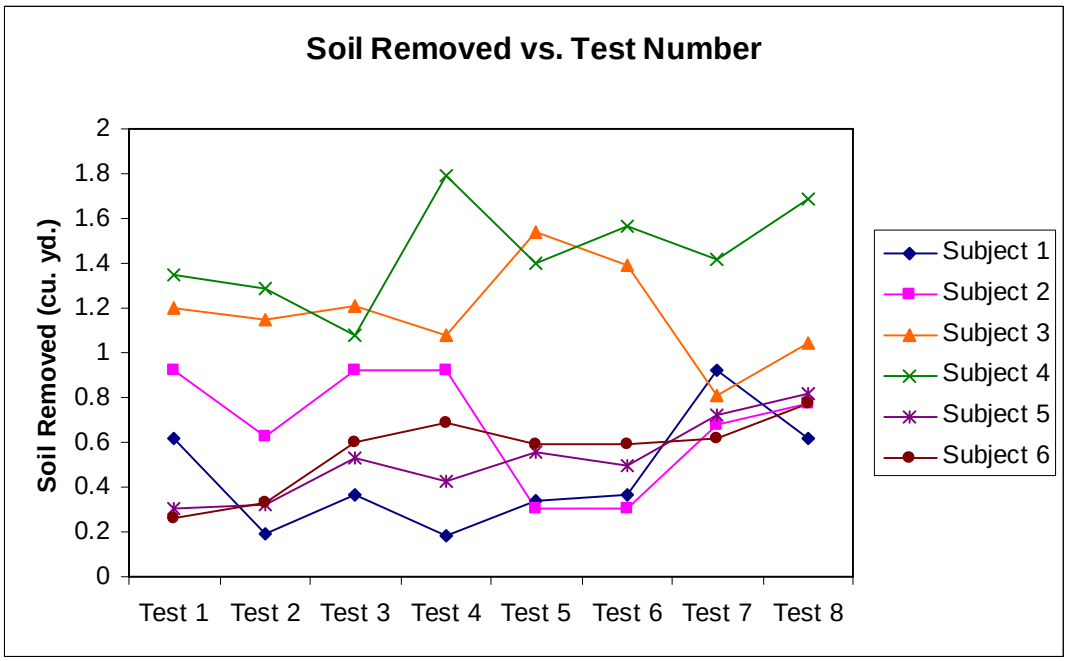

Fig. 41 Soil Removed vs. Test Number.

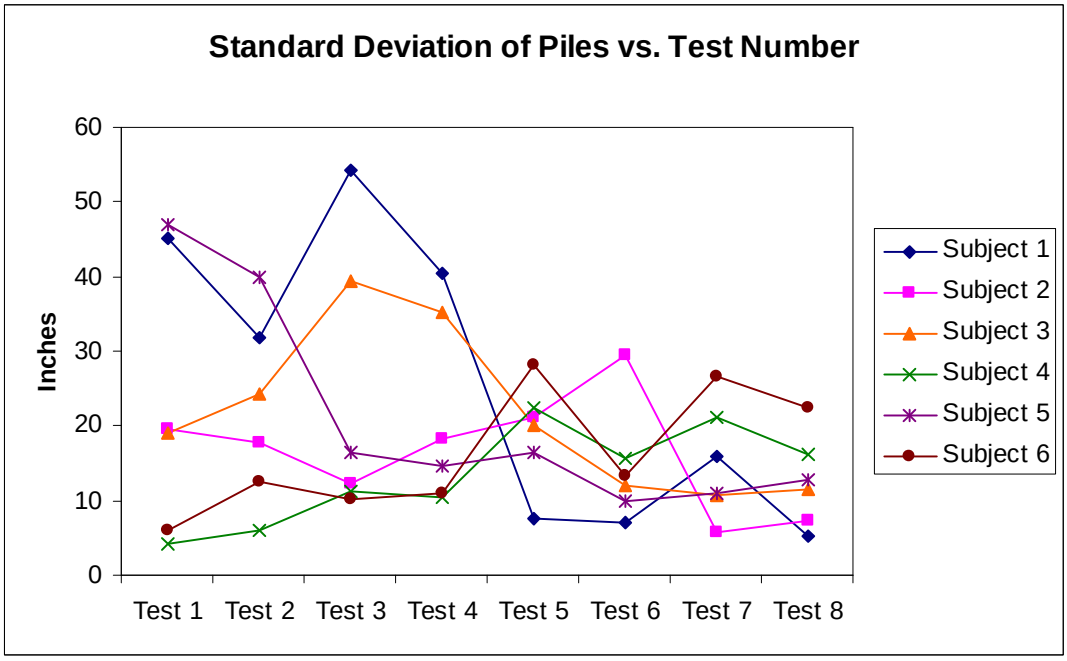

Fig. 42 Standard Deviation of Piles vs. Test Number.

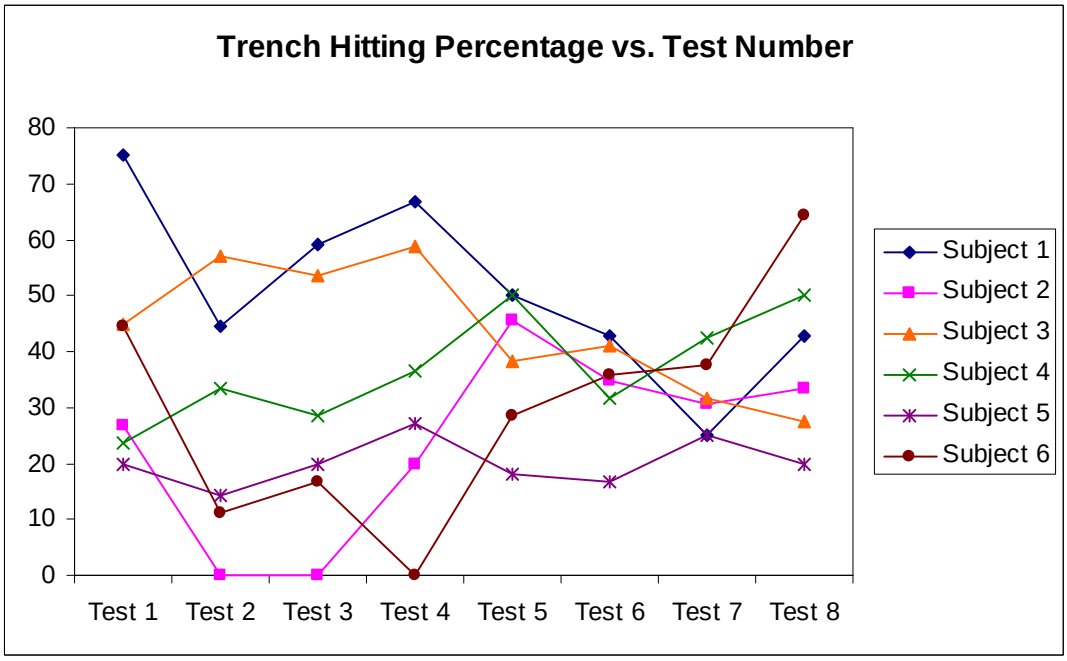

Fig. 43 Trench Hitting Percentage vs. Test Number.

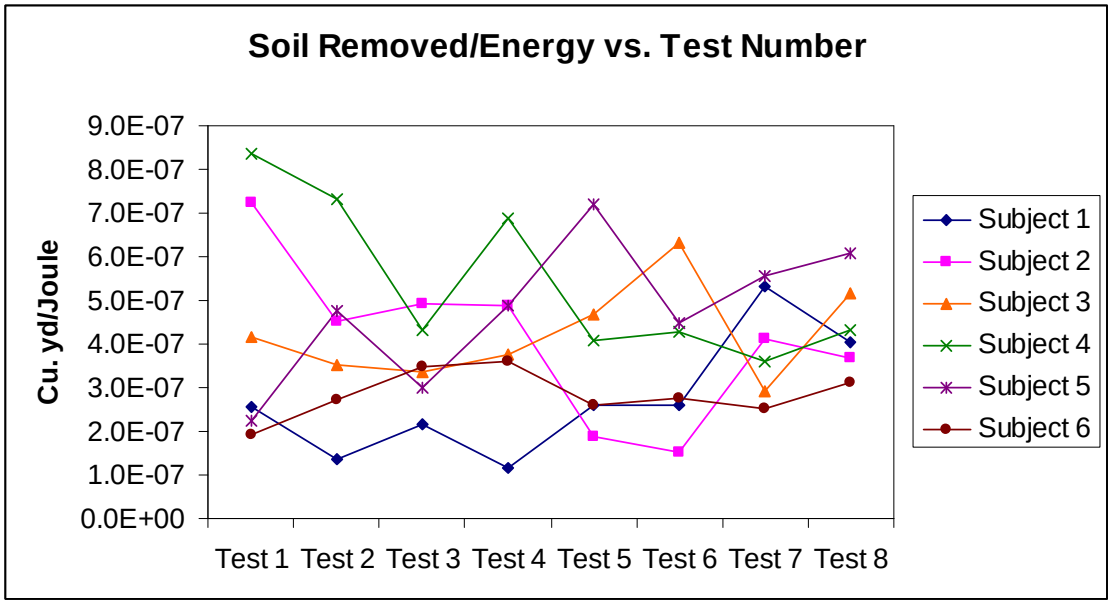

Fig. 44 Soil Removed/Energy vs. Test Number.

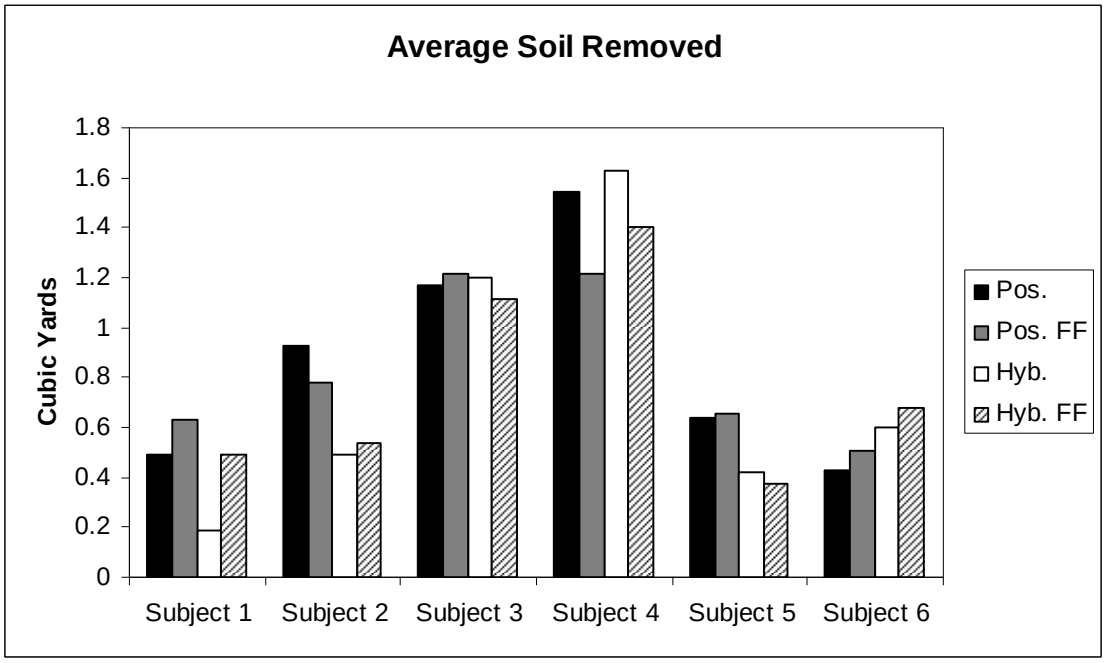

Fig. 45 Average Soil Removed for Each Feedback Scheme.

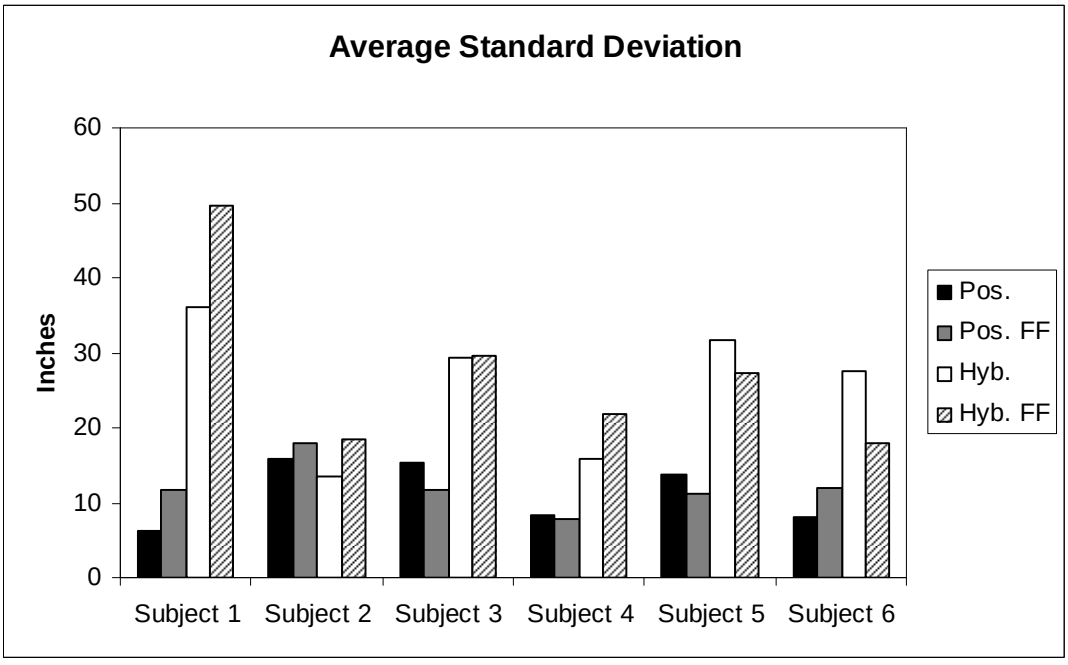

Fig. 46 Average Pile Standard Deviation for Each Feedback Scheme.

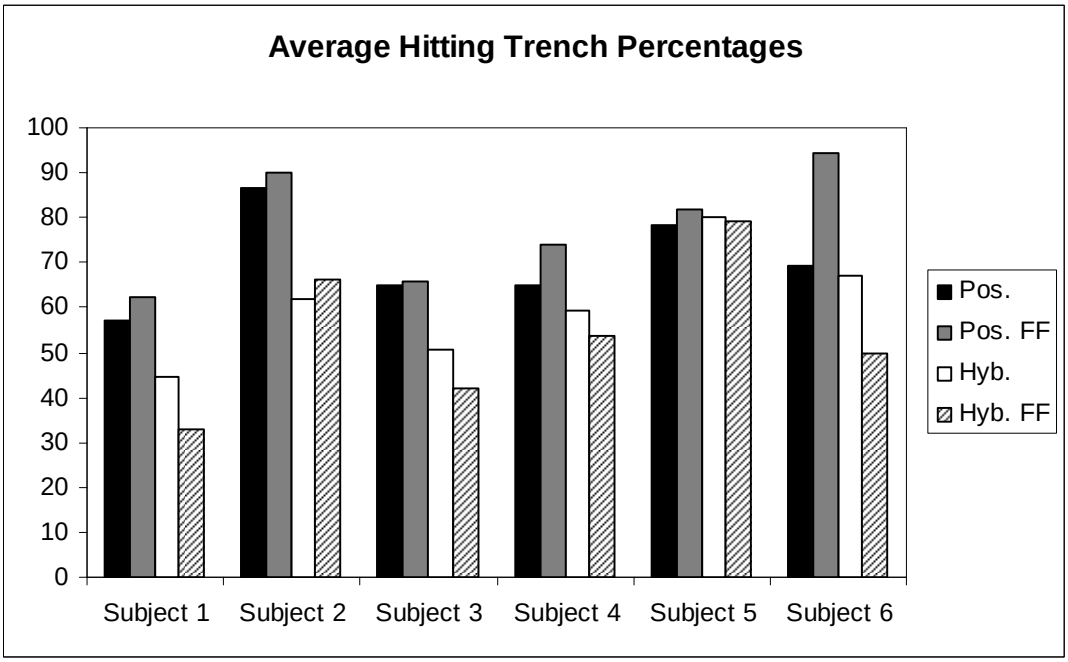

Fig. 47 Average Trench Hitting Percentage for Each Feedback Scheme.

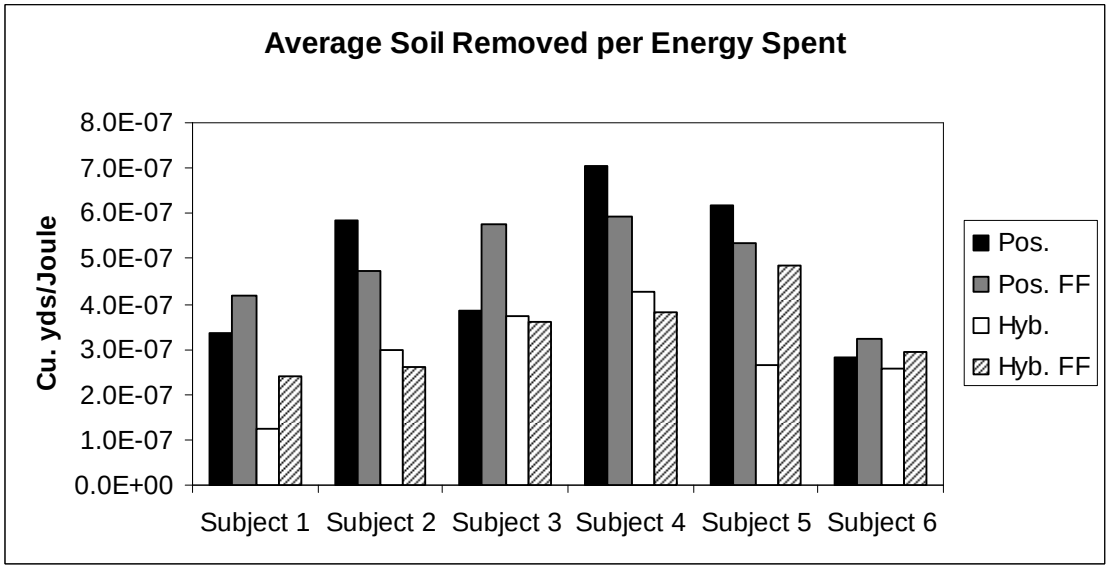

Fig. 48 Average Soil Removed/Energy for Each Feedback Scheme.

REFERENCES

[1] http://www.britannica.com, Jan. 31, 2009.

[2] http://www.merriam-webster.com/dictionary/haptic, Jan. 31, 2009.

[3] HUSCO International, Personal communication with D. Stephenson.

[4] P. D. Lawrence, S. E. Salcudean, N. Sepehri, D. Chan, S. Bachmann, N. Parker, M. Zhou, and R. Frenette, "Coordinated and force feedback control of hydraulic excavators," Proc. of the Intl. Symp. On Experimental Robotics IV, Stanford, CA, pp. 181–194, Jun 1995.

[5] S. E. Salcudean, K. Hashtrudi-Zaad, S. Tafazoli, S. P. DiMaio, and C. Reboulet, "Bilateral matched impedance teleoperation with applications to excavator control," IEEE Control Systems Magazine, vol. 19, pp. 966–971, Dec 1999.

[6] D. W. Johnson, G. H. Lovell, and J. J. Murray, "Development of a coordinated motion controller for a front shovel excavator," Proc. of the Seventh Topical Meeting on Robotics and Remote Systems, Augusta, GA, pp. 239–246, Apr 1997.

[7] A. Barrientos, O. Luengo, and A. Mora, "Teleoperated backhoe excavator with haptic control," Intl. Symp. onAutomation and Robotics in Construction, Madrid, Spain, pp. 491–496, Sept 1999.

[8] N. Parker, S. Salcudean, and P. Lawrence, "Application of force feedback to heavy duty hydraulic machines," Proc. of the Intl. Conf. on Robotics and Automation, Atlanta, GA, pp. 375–381, May 1993.

[9] I. Farkhatdinov and J. Ryu. "Hybrid position-position and position-speed command strategy for the bilateral teleoperation of a mobile robot," Intl. Conf. on Control, Automation and Systems, Oct 17-20 2007, Seoul, South Korea, pp. 2442-2447.

[10] T. Kim, E. Kim and J. Kim. "Development of a humanoid walking command system using a wireless haptic controller," 2008 Intl. Conf. on Control, Automation and Systems, Oct 14-17, 2008, Seoul, South Korea, pp. 1178-1183.

[11] S. E. Salcudean, S. Tafazoli, P.D. Lawrence, and I. Chau, "Impedance control of a teleoperated mini excavator," Proc. of the Intl. Conf. on Advanced Robotics, Monterey, CA, pp. 19-15, July 1997.

[12] M. E. Kontz, "Haptic Control of Hydraulic Machinery Using Proportional Valves," PhD thesis, The Georgia Institute of Technology, G.W. Woodruff School of Mechanical Engineering, 2007.

[13] Bobcat Company, http://bobcat.com, January 22, 2009.

[14] J. Zimmerman, C. Williamson, M. Pelosi, and M. Ivantysynova, "Energy consumption of an LS excavator hydraulic system," Proc. of the ASME IMECE, v 4, pp. 117-126, Nov, 2008.

[15] K.S. Fu, R.C. Gonzalez, and C.S.G Lee. "Robotics: Control, Sensing, Vision, and Intelligence." McGraw-Hill, New York, New York, 1987.

[16] J. Zimmerman. Personal Communications, July 2007 – Jan. 2009.

[17] J. Wang, G. Gong, and H. Yang. "Control of bulk modulus of oil in hydraulic systems," Proceedings of the 2008 IEEE/ASME Intl. Conf. on Advanced Intelligent Mechatronics 2008, Aug 2-5, 2008, Xi'an, China. Pp. 1390-1395.

[18] C. Williamson. Personal Communications, July 2007 – Jan. 2009.

[19] A. Reece, “Fundamental equation of earth-moving mechanics”, Proc. of the Symp. on Earth-Moving Machinery, London, England, vol. 179, n Part 3F, 1964, pp. 16-22

[20] F. Malaguti, “Soil machine interaction in digging and earthmoving automation,” Intl. Symp. on Automation and Robotics in Construction, (Brighton, UK), pp. 187–191, May 1994.

[21] F. Malaguti. “Improved Model of soil for environment-robot excavator interaction”. Proc. of the 16th IEEE Intl. Symp. on Automation and Robotics in Construction. Sept. 1999, Madrid, Spain. pp. 523-527.

[22] C. Tan, Y. Zweiri, K. Althoefer, and L. D. Seneviratne, “Online soil parameter estimation for autonomous vehicles” Proc. of IEEE Intl. Conf. on Robotics and Automation, Sept. 2003, Taipei, Taiwan, pp. 121-126

[23] S. P. DiMaio, S. E. Salcudean, C. Reboulet, “A virtual environment for the simulation and programming of excavation trajectories.” Presence, vol. 10, no. 5, pp. 465-476. MIT Press, Cambridge, Massachusetts.

[24] S. P. DiMaio, S.E. Salcudean, C. Reboulet, S.Tafazoli, and K. Hashtrudi-Zaad, “A virtual excavator for controller development and evaluation,” Proc. of the 1998 IEEE Intl. Conf. on Robotics and Automation, Leuven, Belgium, 1998, pp. 52–58.

[25] M. Elton, W. Book. “Improved Soil Model for Real Time Fixed Step Excavating Simulation,” (paper to be submitted).

[26] A. Koivo. “Fundamental for Control of Robotic Manipulators.” Wiley & Sons, New York, New York, 1989.

[27] Sensable Technologies, http://sensable.com.

[28] H. I. Torres-Rodriguez, V. Parra-Vega, and F.J. Ruiz-Sanchez, "Integration of force-position control and haptic interface facilities for a virtual excavator simulator," Proc. 2005 Intl. Conf. On Advanced Robotics, Seattle, USA, 2005, pp. 761-768.